ROYAL SOCIETY
OF CHEMISTRY

Check for updates

Direct conversion of CO$_2$ to aromatics based on the coupling strategy and multi-functional catalysis

Chang Liu,[a] Yangdong Wang,*[a] Lin Zhang,[a] Junjie Su,[a] Su Liu,[a] Haibo Zhou,[a] Wenqian Jiao[a] and Zaiku Xie ([ID]) *[ab]

As fundamental chemicals and building blocks for the modern chemical industry, aromatics possess a huge market demand. The direct and atom-economic conversion of CO$_2$ to aromatics holds the potential to diminish the reliance on petroleum resources and provides a viable approach towards a net-zero chemical industry. The key lies in the implementation of the highly efficient coupling catalysis strategy and utilization of multi-functional catalysts. In this review, recent advances in the direct conversion of CO$_2$ to aromatics *via* the methanol-mediated pathway and the modified Fischer–Tropsch synthesis route are comprehensively discussed, including an in-depth analysis of the tandem reaction mechanism and bifunctional catalysts, which consist of metal-based materials (including metals, metal oxides, or metal carbides) and zeolites. Furthermore, several novel catalytic pathways, involving coupling CO$_2$ conversion with reactions such as CO hydrogenation, aromatic alkylation, or alkane aromatization, are also elaborated. Subsequently, the coupling effect of multi-functional catalysis, as well as the influence of the proximity between catalytic components, is explored. Moreover, the revealing and construction of the spatial pathway for tandem reactions, which enable the spatio-temporal coupling of multi-functional catalytic systems, are addressed. The challenges and potential directions for the further development of the direct CO$_2$-to-aromatics conversion technology are finally proposed.

Broader context

The conversion and utilization of CO$_2$ is an important pathway for carbon cycling and a pivotal aspect of sustainable energy solutions, representing a cutting-edge area of academic and technological research. Among diverse reaction paths, CO$_2$ hydrogenation to aromatics stands as an alternative approach for production of fundamental chemicals. This process involves a complex tandem reaction network, including C–O activation, C–H bond formation, and C–C coupling, and can be realized utilizing the coupling strategy and multi-functional catalysis. However, uncertainty remains concerning which pathway holds the greatest potential for industrialization. Therefore, a systematic and rigorous analysis of existing advancements is necessary to clarify directions for future progress. Regarding the coupling catalytic strategy, the underlying coupling mechanism, particularly the spatio-temporal effects involving a temporal sequence of reactions across a spatial arrangement of catalytic sites, constitutes the cornerstone of regulating the catalytic performance in CO$_2$ conversion. This review summarizes and analyzes research progress in the direct conversion of CO$_2$ into aromatics based on the coupling strategy and multi-functional catalysis, focusing on the construction of spatio-temporal coupling and directional spatial pathways for tandem reactions. With the continuous development and expansion of the coupling strategy, the realm of CO$_2$ conversion will undoubtedly demonstrate renewed vigor and vitality.

1. Introduction

As indicated by the International Energy Agency, global energy-related carbon dioxide (CO$_2$) emissions have been steadily

[a] State Key Laboratory of Green Chemical Engineering and Industrial Catalysis, SINOPEC Shanghai Research Institute of Petrochemical Technology Co., Ltd, 201208 Shanghai, P. R. China. E-mail: wangyd.sshy@sinopec.com, xzk@sinopec.com

[b] China Petrochemical Corporation (SINOPEC Group), 100728 Beijing, P. R. China

growing over the past five decades and reached a new record of 37.4 Gt in 2023 (Fig. 1).[1,2] Consequently, the emerging environmental issues, particularly global warming and climate change, are threatening the long-term human survival. Hence, it has become a universal consensus to reduce CO$_2$ emissions, and countries such as China have made their net-zero commitments. The key to achieving the net-zero goal lies in the innovation and development of novel pathways for carbon conversion and carbon cycling with high atom economy. Aromatics are pivotal platform chemicals and monomers for

synthetic materials, serving as the building blocks for the chemical and materials industries, with a big market. Thus, the conversion of CO_2 into aromatics using renewable "green hydrogen" has emerged as a promising approach to optimize carbon resource utilization and close the carbon cycle. Compared with the traditional indirect route consisting of the CO_2-to-methanol and methanol-to-aromatics steps, the novel direct route for CO_2-to-aromatics conversion requires a shorter process and improves the theoretical hydrogen atom economy by approximately 11–20%, making it more technically competitive.

The direct conversion of CO_2 to aromatics involves the coupling of diverse reaction steps utilizing multi-functional catalysts. In 2016, Bao *et al.* developed a novel bifunctional catalyst that integrates metal oxides, which are active for CO hydrogenation, with zeolites possessing carbon chain growth activity. This metal oxide/zeolite (OXZEO) catalyst realizes the direct conversion of syngas (CO/H_2) into light olefins with an 80% selectivity for $C_2^=–C_4^=$, surpassing the Anderson–Schulz–Flory (ASF) limitation of approximately 58% for $C_2–C_4$ in
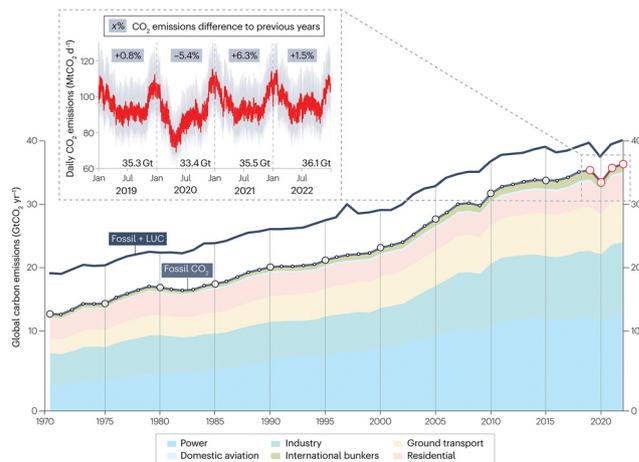

Fig. 1 Global CO_2 emissions during 1970–2022. Reprinted with permission from Liu *et al.* Copyright (2023), Springer Nature Limited.[2]

traditional Fischer–Tropsch synthesis reactions. This coupling reaction strategy using bifunctional catalysts further establishes a crucial foundation for the direct conversion of CO_2 to aromatics, a field of research that has drawn great attention in recent years. Extensive research has been conducted utilizing metal-based materials (including metals, metal oxides, or metal carbides) and zeolites *via* the methanol-mediated or the modified Fischer–Tropsch synthesis pathways. For the methanol-mediated pathway, metal oxide catalysts exhibiting exceptional CO_2 activation and restricted carbon chain growth capabilities, such as Zn–Zr and Zn–Cr binary oxides and zeolite catalysts with tailored acidity, especially ZSM-5, have been developed. Most of these catalysts achieve a CO_2 conversion below 30% and an aromatic selectivity of approximately 80%. Based on the modified Fischer–Tropsch pathway, Fe-based catalysts, including NaZn–Fe and Cu–Fe, have been integrated with the ZSM-5 zeolite. However, a broad product distribution is obtained, due to the relatively uncontrollable carbon chain growth on the surface of the Fe-based catalyst. While CO_2 conversion can exceed 40%, the aromatic selectivity mostly remains below 60%. As a highly active

Chang Liu

Dr Chang Liu received her BS and MS in chemical engineering from Tsinghua University. She joined the SINOPEC Shanghai Research Institute of Petrochemical Technology in 2015, during which she received her PhD in physical chemistry from Fudan University. She is now working as an associate research fellow. Her research interests focus on the design and synthesis of multifunctional catalytic materials, and the application of the coupling catalysis strategy in C1 utilization and production of olefins and aromatics.

Yangdong Wang

Prof. Yangdong Wang got his PhD degree in physical chemistry from Nanjing University in 2000. He then joined the SINOPEC Shanghai Research Institute of Petrochemical Technology. He is currently the chief expert of SRIPT. His research interests focus on the coupling catalysis strategy and industrial catalysis in petrochemical, coal chemical, and green chemistry technologies, including metathesis of C4 olefins, hydrogenation of CO and CO_2 to chemicals, and green catalytic oxidation.

Zaiku Xie

Prof. Zaiku Xie received his PhD from the East China University of Science and Technology. He joined SINOPEC in 1985 and is currently the chief scientist of the Sinopec Group. He was the chief scientist on porous catalytic materials in the National Basic Research Development Program of China from 2003 to 2013. He is an academician of the Chinese Academy of Sciences and a Fellow of the Royal Society of Chemistry. His research interests are mainly focused on the preparation, characterization, and industrial applications of novel zeolite-based catalytic materials.

and extensively studied research field, comprehensive reviews have been published on CO_2-to-hydrocarbon conversion *via* the methanol-mediated or the modified Fischer–Tropsch synthesis routes.[3–9] With the literature corpus expanding and new coupling catalytic routes emerging, this review summarizes recent advancements in the direct conversion of CO_2 into aromatics based on the coupling strategy and multi-functional catalysis. Beyond the methanol-mediated or the modified Fischer–Tropsch synthesis routes, new routes integrating CO_2 conversion with processes, such as CO hydrogenation, aromatic alkylation, or alkane aromatization, are also elaborated. From the new perspective of spatio-temporal coupling catalysis, the underlying coupling effects are clarified, encompassing the impact of spatial proximity between catalytic components. Thus, the rational design principles for multi-functional catalysts are proposed, emphasizing the construction of spatio-temporal coupling and directional spatial pathways for tandem reactions. Then, the trends in CO_2-to-aromatics technology, focusing on the coupling catalytic strategy and spatio-temporal pathway for tandem reactions, are analyzed.

2. Direct conversion of CO_2 to aromatics through the methanol-mediated pathway
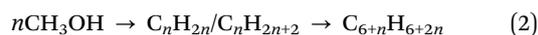
2.1. Reaction mechanism

In the process of direct conversion of CO_2 to aromatics through the methanol-mediated pathway, CO_2 undergoes activation followed by hydrogenation to form the methanol intermediate on the surface of the metal oxide catalyst. Then, the methanol intermediate is transferred to and catalyzed by the zeolite catalyst, resulting in its transformation into aromatics. The corresponding reaction equations are eqn (1) and (2):[4]

CO_2 hydrogenation to methanol:

$$CO_2 + 3H_2 \rightarrow CH_3OH + H_2O \tag{1}$$

Conversion of methanol to aromatics (MTA):

$$nCH_3OH \rightarrow C_nH_{2n}/C_nH_{2n+2} \rightarrow C_{6+n}H_{6+2n} \tag{2}$$

Mechanism of CO_2 hydrogenation to methanol over metal oxide catalysts. The adsorption and activation of CO_2 on the surface of metal oxides have been extensively studied. CO_2 first adsorbs on active sites, such as oxygen vacancies, on the metal oxide surface and then reacts with activated hydrogen species to form the C–H bonds. Fig. 2 illustrates two primary pathways for the hydrogenation of CO_2, the RWGS-CO pathway and the formate pathway.[4] In the RWGS-CO pathway, the *HOCO species derived from CO_2 hydrogenation is transformed into *CO *via* the RWGS reaction. Subsequent hydrogenation of the *CO species results in the formation of *HCO or *COH, which undergoes further hydrogenation to produce methanol. In the formate pathway, CO_2 undergoes a stepwise hydrogenation process *via* *HCOO, *H_2COOH, *H_2CO, *H_2COH or *H_3CO, ultimately leading to the formation of methanol.[4,10]

Mechanism of methanol conversion over zeolites. In the bifunctional catalytic system, the methanol intermediate, formed on the surface of metal oxides, diffuses inside the zeolite pore structure and is further transformed into aromatics catalyzed by the zeolite acid sites. Several theories have been proposed to describe the reaction pathway of C–C bond formation in zeolites, including direct mechanisms such as the oxonium ion mechanism, carbene mechanism, and free radical mechanism, as well as indirect mechanisms represented by the hydrocarbon pool mechanism (Fig. 3A).[11,12] These theories have attracted significant attention and long-term debate. The hydrocarbon pool mechanism, which was first proposed by Dahl *et al.*[13,14] and later developed into the dual-cycle mechanism by Bjørgen *et al.*,[15–17] has been widely investigated. Advancements in characterization techniques and theoretical calculation methods have led to an increasingly sophisticated understanding of the mechanisms underlying different reaction stages in recent years.[18–20] According to the aforementioned theories, the hydrocarbon pool species, composed of long-chain olefins and polymethylbenzenes, are adsorbed on the Brønsted acid sites within the zeolite pore structure.[21–26] Through the processes of oligomerization/cracking with long-chain olefins (olefin-based cycles) or alkylation/dealkylation involving polymethylbenzenes (aromatic-based cycles), methanol is primarily converted into light olefins with a minor yield of aromatics (Fig. 3B).[15,16]
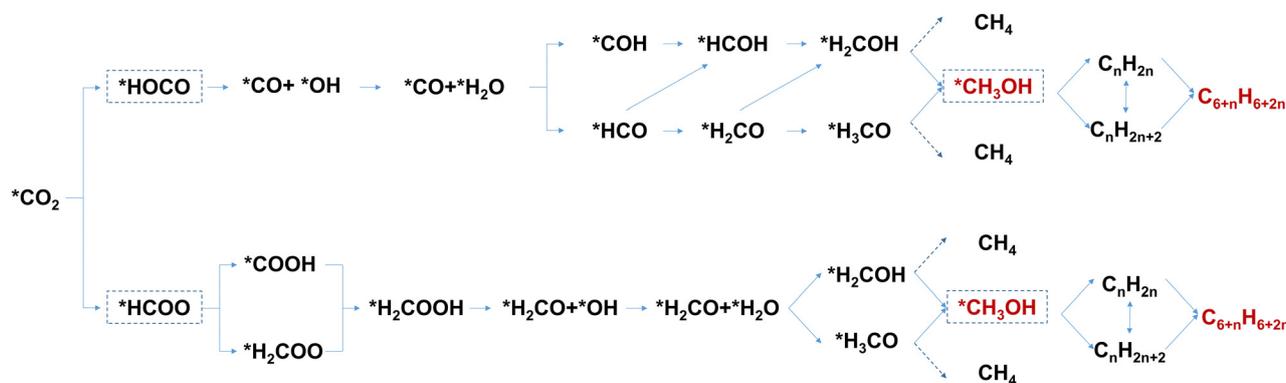

Fig. 2 Reaction pathways for conversion of CO_2-to-aromatics *via* the methanol-mediated route. Reproduced with permission from Wang *et al.* Copyright (2021), Elsevier Inc.[4]
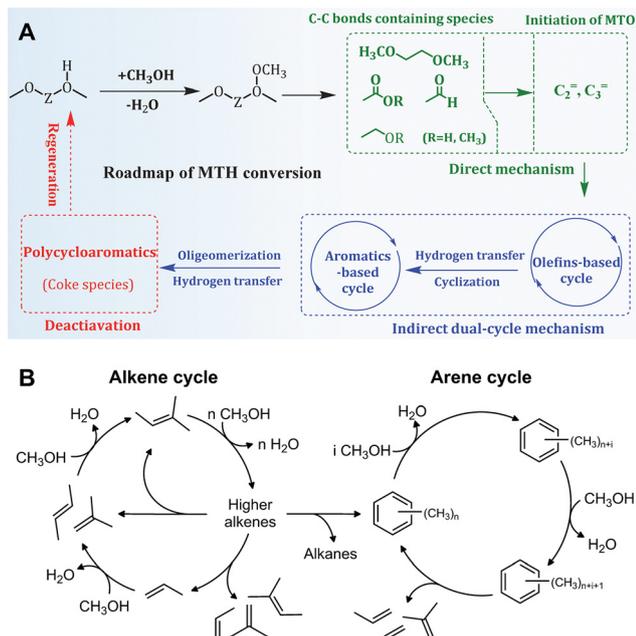
Fig. 3 (A) The induction, steady-state and deactivation stages. Reprinted with permission from Dai *et al.* Copyright (2022), Wiley-VCH GmbH.[11] (B) The modified hydrocarbon pool mechanism, *i.e.*, the dual-cycle mechanism of the methanol conversion reaction in zeolites. Reprinted with permission from Erichsen *et al.* Copyright (2013), Elsevier B.V.[16]

The aromatic products are mainly generated by the aromatization of olefins. Specifically, the olefins, which are the primary products of the hydrocarbon pool, further undergo a series of reactions, including oligomerization, cyclization, and hydrogen transfer/dehydrogenation over the acid sites of zeolites, and are ultimately converted into aromatics.[27–31] Depending on the catalytic system employed, the olefin aromatization reaction proceeds along two distinct pathways. In the Brønsted acid (zeolite) catalytic system, the reaction predominantly follows the hydrogen transfer pathway (Fig. 4A).[32–34] Initially, $C_2^=$–$C_3^=$ olefins are protonated and oligomerized into $C_4^=$–$C_{10}^=$ olefins, which are subsequently transformed into dienes and alkanes through
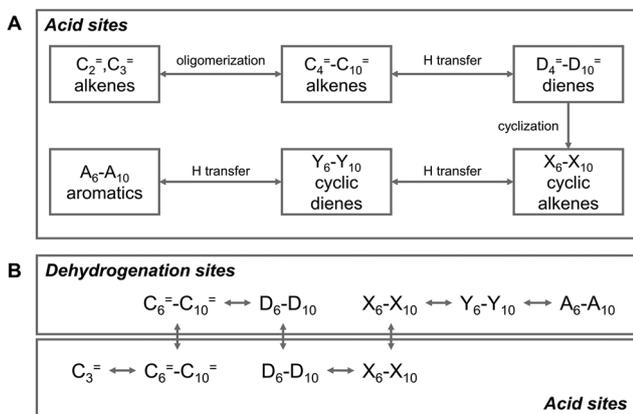

Fig. 4 The aromatization of olefins over (A) ZSM-5 and (B) metal-ZSM-5. Reproduced with permission from Lukyanov *et al.* Copyright (1995), American Chemical Society[33] and Caeiro *et al.* Copyright (2006), Elsevier B.V.[34]

hydrogen transfer. Then, the cyclization (intramolecular oligomerization) of dienes results in the formation of cyclic olefins, which undergo further hydrogen transfer to produce cyclic dienes. Aromatics are finally obtained through hydrogen transfer of the cyclic dienes.[35,36] Characterized by multiple hydrogen transfer reaction steps, this pathway generates a large amount of alkanes as by-products. However, due to their low reactivity, these alkanes are difficult to further convert into aromatics, thereby limiting the aromatic selectivity of this reaction pathway.[37] Upon the introduction of a metallic or Lewis acid center into the Brønsted acid zeolite, the synergy between Lewis and Brønsted acid sites shifts the reaction from the hydrogen transfer pathway to the dehydrogenation pathway (Fig. 4B), greatly enhancing the reaction activity and aromatic selectivity.[32–34]

Until recently, the hydrocarbon pool mechanism and olefin aromatization mechanism have been successfully employed to elucidate the CO/CO_2-to-olefins/aromatics/gasoline reactions *via* the methanol-mediated pathway.[30,38–43] However, significant differences exist between the coupling reaction of CO_2-to-aromatics and the methanol conversion reaction, including the co-existence of two distinct catalytic components namely metal oxides and zeolites, the high-pressure environment of CO_2 and H_2, varying concentrations of methanol as either an intermediate or a reactant, and potential differences in the structure and composition of hydrocarbon pool species. These factors collectively contribute to variations in the reaction mechanisms. Specifically, Yang *et al.* recently proposed an initial aldol-cycle, which is closely linked to the dual-cycle with the participation of both Brønsted and Lewis acid sites (Fig. 5A).[44] Arslan *et al.* identified oxygenated hydrocarbon pool species in the CO/CO_2-to-aromatics reaction and put forward an "aldol-aromatic" mechanism (Fig. 5B).[45] According to this mechanism, in the metal oxide/zeolite bifunctional catalytic system, species such as CH_3O^* and CH_xO^* generated on the metal oxide surface are transferred to and converted into aldol condensates *via* the aldol reaction pathway within the zeolite. The aldol species are then transformed into cyclic oxygenates, namely phenols, ketones, and cyclic aldehydes, through intermolecular or intramolecular cyclization. Ultimately, these cyclic oxygenates are converted into single-ring polymethylbenzene through the "aldol–phenol–aromatic" cycle, which is referred to as the "aldol–aromatic" mechanism.

Alongside the main reaction sequence of CO_2 conversion to methanol and subsequently to aromatics, this tandem reaction is accompanied by a series of side reactions. On the one hand, through the RWGS reaction, CO_2 can react with H_2 and generate H_2O and CO on the metal oxide surface, which reduces the carbon conversion efficiency. The existence of H_2O may even induce structural changes in both the metal oxides and zeolite catalysts. On the other hand, long-chain products may either crack into smaller hydrocarbons, which is unfavorable for aromatization,[42,46–48] or undergo intensive condensation, leading to coke deposition and catalyst deactivation.[42,48,49] Typical deactivating species and their formation routes in the methanol conversion reaction system have been proposed, as shown in Fig. 6.[22,50–52] Other side reactions, such as isomerization and alkylation, are correlated with the spatial positioning of zeolite
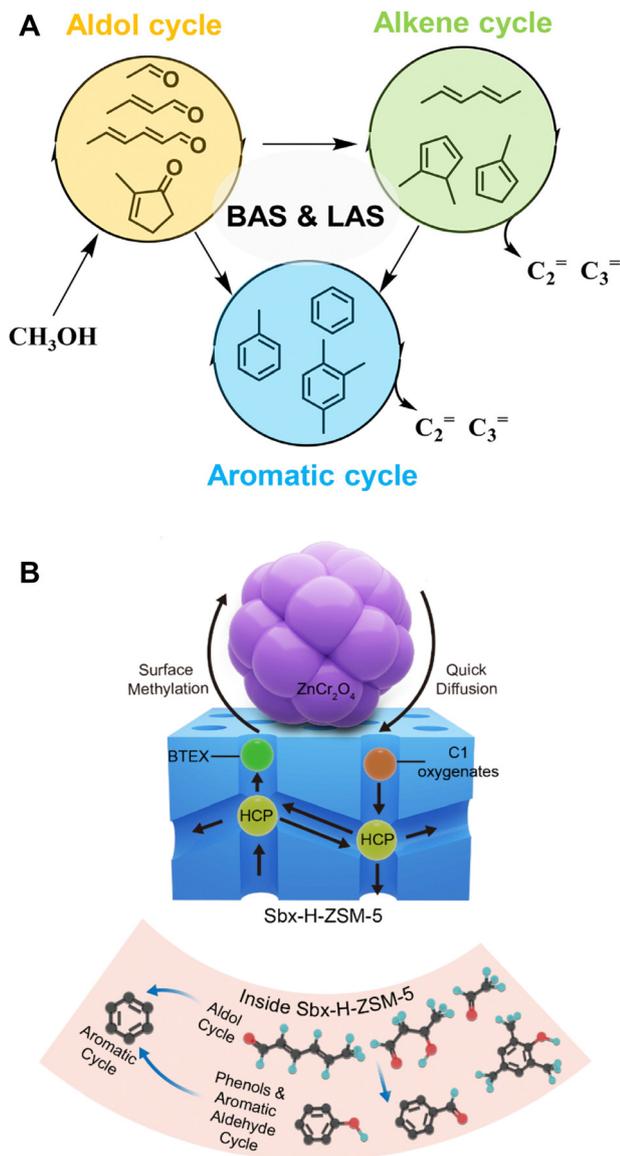
A

Aldol cycle

Alkene cycle

BAS & LAS

CH_3OH

$C_2^=$ $C_3^=$

$C_2^=$ $C_3^=$

Aromatic cycle

B

Surface Methylation

Quick Diffusion

$ZnCr_2O_4$

BTEX

C1 oxygenates

HCP

HCP

Sbx-H-ZSM-5

Inside Sbx-H-ZSM-5

Aromatic Cycle

Aldol Cycle

Phenols & Aromatic Aldehyde Cycle

Fig. 5 (A) The "aldol–alkene–aromatic" triple-cycle mechanism. Reprinted with permission from Yang *et al.* Copyright (2022), KeAi.[44] (B) The "aldol–phenol–aromatic" cycle, *i.e.*, the "aldol–aromatic" mechanism. Reproduced with permission from Arslan *et al.* Copyright (2022), American Chemical Society.[45]

acid sites and significantly influence the aromatic distribution.[41,43,53–56] Furthermore, deep hydrogenation of intermediates or products into alkanes also occurs, either through the activated hydrogen species on the metal oxides, or through hydrogen transfer over the Brønsted acid sites of zeolites.[30,49,57]

### 2.2. Metal oxide/zeolite bifunctional catalysts

2.2.1. Metal oxide catalysts. For the CO_2-to-aromatics reaction catalyzed by metal oxide/zeolite bifunctional catalysts, the matching and synergy between CO_2 hydrogenation and aromatization activities are pivotal to achieving optimal catalytic performance. As CO_2 hydrogenation over metal oxides is the primary step in the tandem reaction, various metal oxide catalysts, such as Cr_2O_3,

$ZnCrO_x$, $ZnAlO_x$, $ZnZrO_x$, $Ga–ZnZrO_x$ and $In_2O_3–ZnZrO_x$ have been developed, based on the identification and enhancement of active sites. The respective catalytic performances are listed in Table 1.

Chromium oxide (Cr_2O_3) and spinel-structured oxides including $ZnCrO_x$ and $ZnAlO_x$. As demonstrated in the study conducted by Wang *et al.*, the abundant oxygen vacancies in Cr_2O_3 nanoparticles promote the activation of C–O bonds, thereby facilitating the formation of CO_2^* intermediates and the production of methanol through the formate pathway.[54,55] Enhancing oxygen vacancy formation is a common strategy for modifying metal oxide catalysts, which can be achieved through the synthesis of structures with high porosity and defect content or through the doping/loading of another metal as a promoter. For example, the incorporation of Zn into Cr_2O_3 not only enhances the adsorption and dissociation of H_2 at the Zn–O site, but also accelerates the formation of oxygen defects. The formation of oxygen vacancies is particularly favored in non-stoichiometric spinel structures, which exhibit a notably random distribution of metallic cations.[66–70] Furthermore, pretreatment with H_2 can remove specific oxygen atoms and further facilitate the formation of surface oxygen defects, thereby enhancing both CO_2 adsorption and conversion (Fig. 7A–J).[43] $ZnCrO_x$, as the first commercial methanol synthesis catalyst, demonstrates excellent resistance to sulfide impurities and high activity for CO/CO_2 hydrogenation at elevated temperatures. Recently, $ZnCrO_x$ has also exhibited outstanding performance in syngas[66,71–73] and CO_2 conversion reaction systems.[43,58] During the transformation of CO_2 over $ZnCrO_x$, intermediate species such as $HCOO^*$ and CO_3^{2-*} are formed, ultimately leading to the formation of methanol, as evidenced by *in situ* characterization.[43,58] $ZnAlO_x$, another typical spinel-structured metal oxide, has also been employed in the CO_2-to-aromatics reaction (Fig. 7K–N).[41] By combining a nano-$ZnAlO_x$ spinel with nano-ZSM-5 having a high Si/Al ratio, a selectivity of 73.9% for aromatics can be achieved. In this bifunctional catalytic system, CO_2 is hydrogenated to formate species at the Zn^{2+} sites of $ZnAlO_x$ and subsequently hydrogenated into methanol. Afterwards, methanol is dehydrated at the AlO_x sites to form dimethyl ether, which is identified as another potential intermediate besides methanol.

Metal oxides with solid solution structure. The $ZnO–ZrO_2$ solid solution has shown excellent performance in the CO_2 hydrogenation to methanol, facilitated by adjacent Zn–Zr dual-sites, which simultaneously activate H_2 and CO_2, respectively (Fig. 8A–D).[74] It has also been employed in the CO_2-to-aromatics reaction after combining with ZSM-5.[53,59,60,62] For example, Li *et al.* achieved a 73% selectivity to aromatic at a 14% CO_2 conversion over ZnZrO/ZSM-5.[60] The CH_xO species derived from the activation and reaction of CO_2 and H_2 over ZnZrO have been determined as the intermediates in the tandem reaction, according to a series of characterization methods, including *in situ* diffuse reflectance infrared Fourier transform spectroscopy (DRIFTS), chemical trapping, and the *in situ* capture of CH_xO by SBA-15 functionalized with an –NH_2 group. Zhou *et al.* reported the synthesis of a $ZnO–ZrO_2$ aerogel
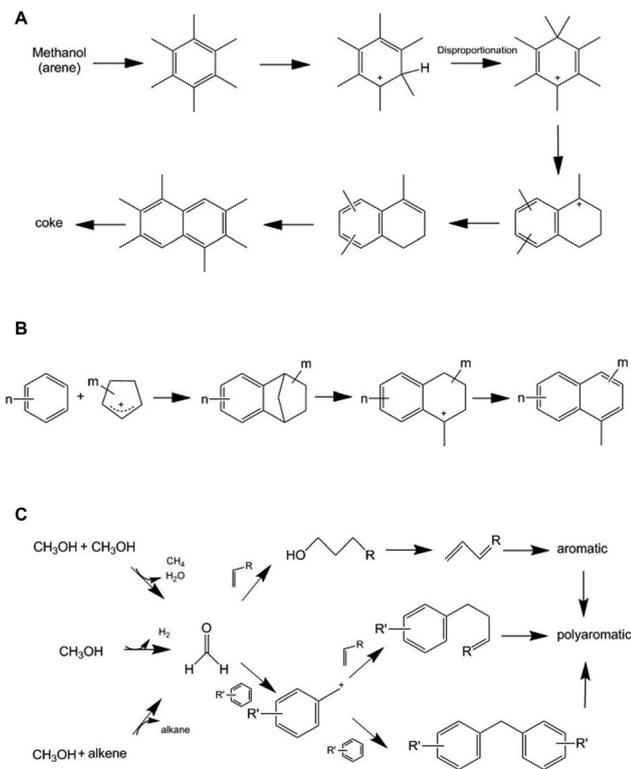
Fig. 6 Typical deactivating species and their formation routes. (A) Dihydro-trimethylnaphthalene and coke species resulting from the rearrangement of heptamethylbenzene ions. (B) Naphthalene generated by the reaction between aromatics and cyclopentenyl cations. (C) Formaldehyde generated from hydrogen transfer or dehydrogenation of methanol, and coke formation resulting from alkylation of olefins and aromatics by formaldehyde. Reprinted with permission from Bjørgen et al. Copyright (2003), Elsevier Science (USA),[22] Wang et al. Copyright (2020), Wiley-VCH Verlag GmbH & Co. KGaA, Weinheim,[51] Hwang et al. Copyright (2019), American Chemical Society,[52] and Li et al. Copyright (2021), The Authors.[50]

using a combined sol–gel and subsequent supercritical drying method (Fig. 8E).[62] Compared with the ZnZrO$_x$ oxides prepared by methods of impregnation, co-precipitation, or hard templating, the ZnO–ZrO$_2$ aerogel has a loose structure characterized by the co-existence of mesopores and macropores, leading to a higher surface area and a larger amount of oxygen vacancies (Fig. 8F–K). A strong correlation between the oxygen vacancy density and the formation rate of methanol is further demonstrated (Fig. 8L), thereby confirming the surface oxygen vacancies as the active sites for the adsorption and activation of CO$_2$. H$_2$–D$_2$ exchange experiments indicate Zn as the active sites for H$_2$ dissociation, and the synergy between ZrO$_2$ and ZnO within the ZnO–ZrO$_2$ solid solution is then proposed. By modification of the ZnZrO$_x$ solid solution with indium or gallium, the formation of oxygen vacancies is promoted and the adsorption and activation of CO$_2$ are therefore enhanced.[64,65] Moreover, the synergistic sites of Zn–Zr can also be constructed from metal–organic frameworks (MOFs). Tian et al. utilized the Zr-containing UIO-66 as a carrier and introduced Zn, Ga, and In by the physical mixing method.[63] Among all, Zn-UIO-66 exhibits superior performance in the conversion of CO$_2$ to aromatics when coupled with ZSM-5, achieving a 21.2% CO$_2$ conversion and an 84.9% selectivity to benzene, toluene, and xylene (BTX). As shown in Table 1, the Cr- and Al- based metal oxides are characterized by a high CO selectivity of 35–91%, while the Zr-based metal oxides show a significantly lower CO selectivity of 10–45%, thus showing superiority in the spacetime yield (STY) of aromatics.

2.2.2. Zeolite catalysts. The structural topology and acidic properties of the zeolite framework constitute the foundation for shape-selective catalysis. ZSM-5 has the MFI topology, featuring adjustable acidity and two sets of intersecting 10-membered ring (10-MR) channels. The dimensions of these 10-MR channels, 5.5 × 5.1 Å for the sinusoidal channel along the a-axis and 5.6 × 5.3 Å for the straight channel along the b-axis, closely resemble those of aromatic rings (5.5 Å). Furthermore, the intersections of these 10-MR channels have a larger space of approximately 10 Å, which favors the formation of aromatics. Consequently, ZSM-5 is an ideal catalyst for the

Table 1 CO$_2$-to-aromatics conversion performance of metal oxides/zeolites through the methanol-mediated pathway

| Catalyst	Temperature (°C)	Pressure (MPa)	Feedstock	Space velocity (mL g^{-1} h^{-1})	CO$_2$ conv. (%)	CO Sel. (%)	Aro. Sel. (%)	Aro. STY (mmol C g^{-1} h^{-1})	Ref.
Cr$_2$O$_3$/H-ZSM-5	350	3	H$_2$/CO$_2$ = 3	1200	33.6	41.2	70.5	1.87	55
Cr$_2$O$_3$ + Zn–ZSM-5@SiO$_2$	350	3	H$_2$/CO$_2$/Ar = 70.25/26.5/3.25	1200	22.1	35.1	70.1	1.43	54
ZnCrO$_x$-ZnZSM-5	320	5	H$_2$/CO$_2$/N$_2$ = 72/24/4	2000	19.9	70.2	56.5	0.75	58
ZnCrO$_x$/ZSM-5	330	3	H$_2$/CO$_2$ = 3	3000	17.5	38.1	64.6	2.34	43
ZnCr$_2$O$_4$/ZSM-5	275	2	H$_2$/CO$_2$ = 3	300	17.4	90.7	79.9	0.04	45
ZnCr$_2$O$_4$/ZSM-5	350	2	H$_2$/CO$_2$ = 3	300	37.48	85	48.1	0.09	45
ZnAlO$_x$&ZSM-5	320	3	H$_2$/CO$_2$/Ar = 3/1/0.2	2000	9.1	57.4	73.9	0.61	41
ZrO$_2$–Cr/ZSM-5@SiO$_2$	360	4	H$_2$/CO$_2$/Ar = 71.95/24.02/4.03	1200	13.9	29	76.8	0.97	56
ZnO/ZrO$_2$-ZSM-5	340	3	H$_2$/CO$_2$ = 3	4800	9.1	42.5	70	1.96	59
ZnZrO/HZSM-5	320	4	H$_2$/CO$_2$/Ar = 72/24/4	1200	14.1	44	73	0.77	60
ZnZrO$_x$/1Mg-3T-ZSM-5	320	2	H$_2$/CO$_2$ = 3	4800	6.6	32.1	∼65	1.56	61
ZnO–ZrO$_2$ Aerogels/H-ZSM-5	340	4	H$_2$/CO$_2$ = 3	7200	16	34.3	76	6.42	62
ZnZrO$_x$/ZSM-5	315	3	H$_2$/CO$_2$/N$_2$ = 72/24/4	1020	17.5	23.8	60.3	0.88	53
6% Zn-UIO-662/Z5	320	3	H$_2$/CO$_2$ = 3	4800	21.2	32.8	88.8	6.78	63
In$_2$O$_3$–ZnZrO$_x$/ZSM-5	320	3	H$_2$/CO$_2$ = 3	4000	22.4	11	92.1	8.20	64
Ga–ZnZrO$_x$/ZSM-5	340	3	H$_2$/CO$_2$ = 3	6000	14.7	23.6	88.1	6.63	65
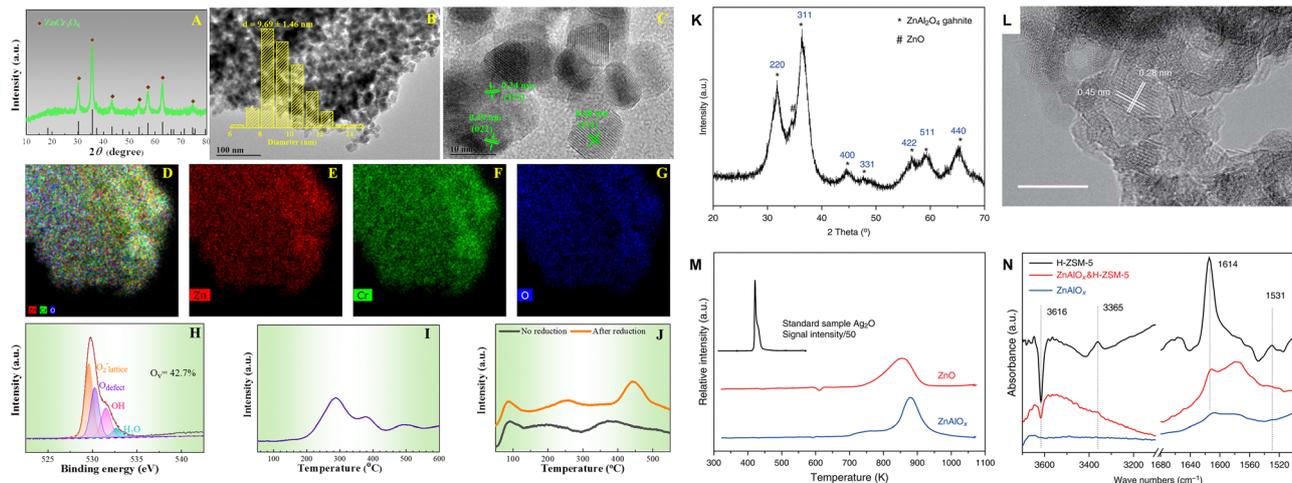
Fig. 7 Morphology, structure and property of the $ZnCrO_x$ and $ZnAlO_x$ spinels. (A) XRD pattern, (B) TEM image, (C) HR-TEM image, (D)–(G) STEM-EDX elemental mapping, (H) O 1s XPS spectra, (I) H_2-TPR profile, and (J) CO_2-TPD profile of the $ZnCrO_x$ oxide. Reprinted with permission from Guo *et al.* Copyright (2024), American Chemical Society,[43] (K) XRD pattern, (L) HR-TEM image with a scale bar of 10 nm, (M) H_2-TPR profiles normalized by weight and the relative intensity of the standard sample Ag_2O was divided by 50, (N) FTIR subtraction spectra relative to adsorption of DTBPy of the $ZnAlO_x$ oxide. Reprinted with permission from Ni *et al.* Copyright (2018), The Authors.[41]

CO_2-to-aromatics reaction. Numerous studies have been reported to optimize product distribution and enhance catalytic performance by modification of zeolite acidity and morphology.

The strength, density and type of acid sites. As the rate-determining step in the formation of aromatics, the dehydrogenation and cyclization reactions exhibit high activation energies, *e.g.* 207 and 230 kJ mol^{-1} for dehydrogenation of ethane and butane, respectively.[75] Thus, a high acid strength of the
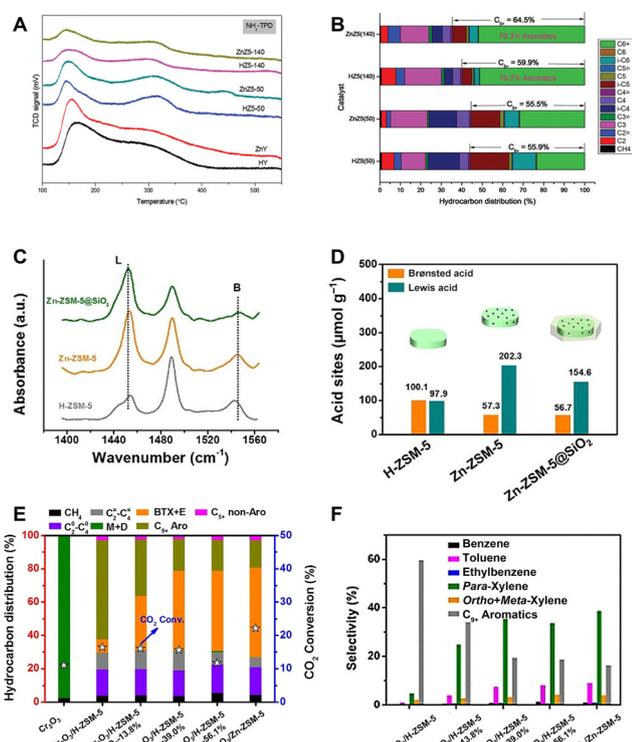
active site is required. The acid strength of silicon–aluminum zeolites, including ZSM-5, is strongly correlated with their Si/Al ratio.[76,77] On the one hand, the Si–OH–Al bridging hydroxyl groups, which compensate for the negative charge of the AlO_4 tetrahedron, are the source of Brønsted acidity. On the other hand, the electron donating effect of the AlO_4 tetrahedron may weaken the acid strength of the bridging hydroxyls, particularly at a high content of adjacent aluminum, or equivalently, at a relatively low Si/Al ratio.[76,77] Consequently, with the increase of
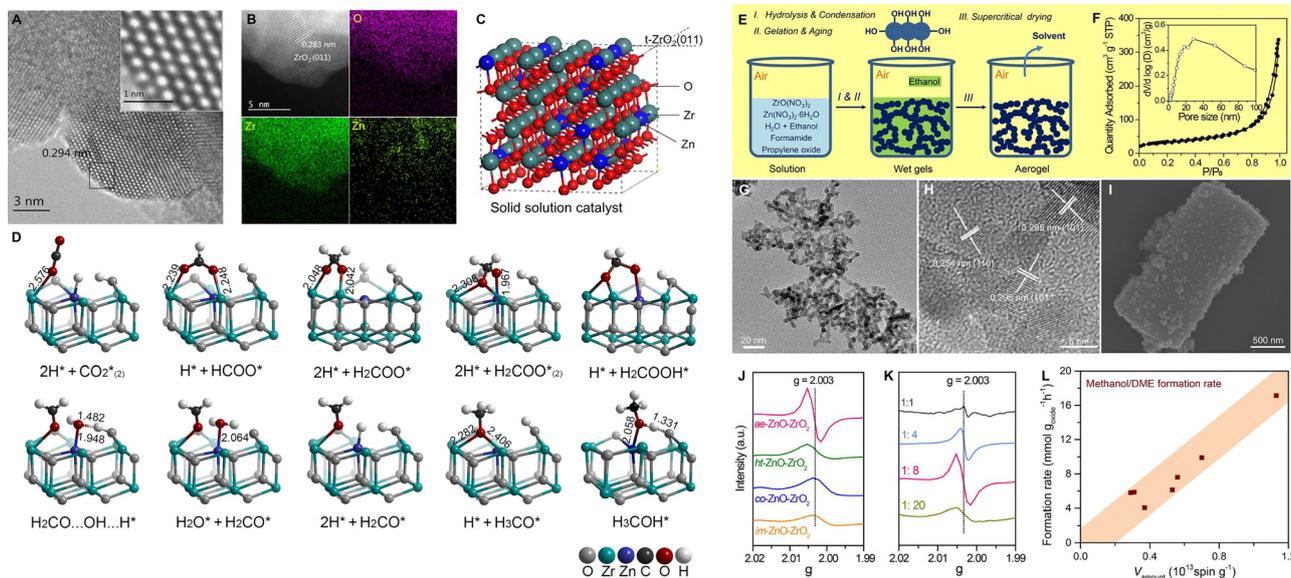
Fig. 8 (A) HRTEM, (B) aberration corrected scanning TEM-high-angle annular dark-field images and elemental distribution of 13% $ZnO-ZrO_2$, (C) schematic description of the $ZnO-ZrO_2$ solid solution catalyst mode and (D) CO_2 hydrogenation reaction path on the (101) surface of the tetragonal $ZnO-ZrO_2$ model by DFT calculations. Reprinted with permission from Wang *et al.* Copyright (2017), the Authors,[74] (E) preparation of the $ZnO-ZrO_2$ aerogel by the sol–gel and subsequent supercritical drying methods, (F) N_2 physisorption analysis of the $ZnO-ZrO_2$ aerogel after calcination, (G) TEM, (H) HRTEM, and (I) SEM images. EPR spectra of $ZnO-ZrO_2$ catalysts with (J) different preparation methods and (K) Zn/Zr ratios. (L) The correlation between oxygen vacancy density and the formation rate of methanol. Reprinted with permission from Zhou *et al.* Copyright (2020), American Chemical Society.[62]

Open Access Article. Published on 09 Nisan 2025. Downloaded on 5.05.2026 00:38:02.
This article is licensed under a Creative Commons Attribution-NonCommercial 3.0 Unported Licence.
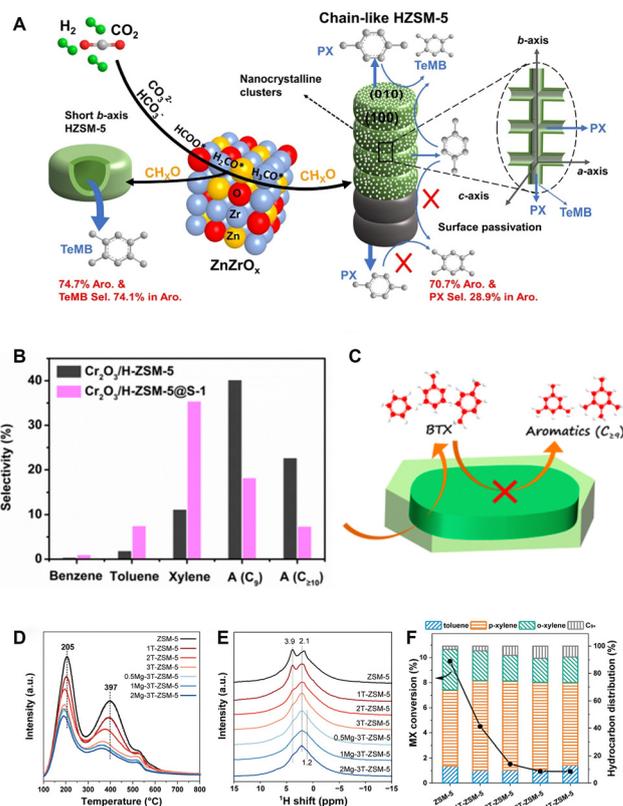
the Si/Al ratio, the acid density decreases, whereas the acid strength especially the Brønsted acid strength intensifies. A series of studies have investigated the effect of zeolite acidity on the catalytic performance of $ZnZrO_x$/ZSM-5 and $ZnCrO_x$/ZSM-5 in the CO_2-to-aromatics reaction.[43,58–60] The non-acidic silicalite-1 zeolite shows negligible carbon chain growth activity.[59] The combination of relatively low acid density and high acid strength at a high Si/Al ratio promotes the formation of C_{5+} products, particularly aromatics.[58] However, excessive acidity will exacerbate the deep hydrogenation of olefins and inhibit the carbon chain growth and aromatization reaction, thus leading to the formation of alkane by-products (Fig. 9A and B).[58] In addition to adjusting the acid strength and density through the Si/Al ratio, introducing metals, such as Zn, as Lewis acid sites into ZSM-5 by methods like ion exchange, can facilitate the dehydrogenation and cyclization of olefins. This process is assisted by the dehydrogenation activity of Lewis acids and their synergy with adjacent Brønsted acid sites.[54,58,78] Wang et al. modified the Cr_2O_3/ZSM-5 bifunctional catalyst by doping ZSM-5 with Zn ions, leading to the formation of $(ZnOH)^+$ Lewis acid sites and precise manipulation of the B/L acid distribution to enhance the synergy between Brønsted and Lewis acid sites, which achieves a para-xylene selectivity of 38.7% at a CO_2 conversion of 22.1% (Fig. 9C–F).[54]

The spatial positioning of acid sites. The spatial distribution of acid sites is another crucial factor influencing catalytic performance, in addition to the strength, density and type of acid sites. Liu et al. identified the b-axis length of ZSM-5 as the key morphology parameter governing aromatic distribution in the syngas-to-aromatics reaction. The strong linear correlation is revealed between the reciprocal of the b-axis length (1/b) and S_{C9+}/A, an indicator of the relative activity of alkylation to aromatization.[79] Wang et al. applied the ZSM-5 zeolite with various morphologies to the CO_2-to-aromatics reaction in combination with $ZnZrO_x$.[53] The chain-like ZSM-5 with a large b-axis size and low external acidity obtains a high selectivity to para-xylene, while the hollow ZSM-5 with a much smaller b-axis size and higher external acidity favors the formation of tetramethylbenzene. The selectivity to xylene and tetramethylbenzene reaches 28.9% and 74.1%, respectively (Fig. 10A). Furthermore, the external acidity of ZSM-5 can be partially eliminated by silanization via chemical liquid deposition or epitaxial growth of an inert silicalite-1 shell (Fig. 10B and C).[55] Additionally, the opening of the 10-MR pores can be narrowed by MgO modification (Fig. 10D–F).[61] Both methods enhance the

Fig. 9 (A) NH_3-TPD profiles of ZSM-5 samples with various Si/Al ratios, and with and without Zn-exchange, and (B) their catalytic performances when combined with $ZnCrO_x$. Reprinted with permission from Zhang et al. Copyright(2019), The Royal Society of Chemistry.[58] (C) FTIR spectra of adsorbed pyridine and (D) densities of B and L acid sites on H-ZSM-5, Zn-ZSM-5, and Zn-ZSM-5@SiO_2. (E) and (F) Catalytic performances of Zn modified ZSM-5. Reprinted with permission from Wang et al. Copyright (2019), Wiley-VCH Verlag GmbH & Co. KGaA, Weinheim.[54]

Fig. 10 (A) Utilization of ZSM-5 with chain-like and hollow morphology in the CO_2-to-aromatics reaction. Reprinted with permission from Wang et al. Copyright (2021), Elsevier B.V.[53] (B) and (C) Catalytic performance of the core−shell structured ZSM-5@S-1 in the CO_2-to-aromatics reaction. Reprinted with permission from Wang et al. Copyright (2019), American Chemical Society.[55] (D) NH_3-TPD profiles, (E) ^{1}H NMR spectra and (F) isomerization of meta-xylene of ZSM-5 co-modified with MgO and an inert shell. Reprinted with permission from Qu et al. Copyright (2023), The Royal Society of Chemistry.[61]
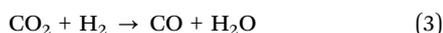
shape-selectivity and inhibit side reactions, such as alkylation and isomerization, thereby contributing to an optimized aromatic distribution, especially a high fraction of light aromatics.[41,54–56,61] For example, Wang et al. synthesized a ZSM-5@silicalite-1 core–shell structured zeolite.[55] By precisely adjusting the shell thickness to minimize the external acidity while ensuring smooth diffusion of intermediates and products, they improved the BTX selectivity from 13.2% to 43.6%, with the para-xylene selectivity increasing from 7.6% to 25.3% over the Cr_2O_3/ZSM-5 bifunctional catalyst. Guo et al. compared the kinetics of the methylation reaction occurring at acid sites located at the intersection of two sets of 10-MR channels and those positioned inside the straight channels within the ZSM-5 framework by DFT calculation.[43] Compared with the acid sites within the straight channels, those at the channel intersections provide a suitably larger reaction space and less steric hindrance, therefore favoring the formation of trimethylbenzene while inhibiting its further methylation. Based on this finding, they designed a $ZnCrO_x$/H-ZSM-5 catalyst and realized the direct and highly selective conversion of CO_2 to trimethylbenzene and ethylene. At a 17.5% CO_2 conversion, the aromatic selectivity reaches 64.6%, 57.4% of which is trimethylbenzene.

3. Direct conversion of CO_2 to aromatics through the modified Fischer–Tropsch pathway
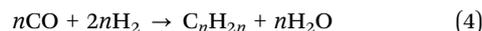
3.1. Reaction mechanism

In the modified Fischer–Tropsch pathway, CO_2 is first transformed into CO by the RWGS reaction over the metal-based catalyst, which then undergoes the Fischer–Tropsch reaction, yielding olefins as intermediates. The aromatization of olefins then occurs over the zeolite catalyst. These reactions follow eqn (3)–(5):[4]
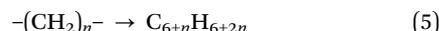
Reverse water–gas shift reaction (RWGS):

$$CO_2 + H_2 \rightarrow CO + H_2O \tag{3}$$

Fischer–Tropsch synthesis (FTS):

$$nCO + 2nH_2 \rightarrow C_nH_{2n} + nH_2O \tag{4}$$

Aromatization of olefins:

$$-(CH_2)_n- \rightarrow C_{6+n}H_{6+2n} \tag{5}$$

Mechanism of the Fischer–Tropsch synthesis over metal-based catalysts. CO_2 is first adsorbed on the RWGS active sites, e.g. Cu or Fe_3O_4, forming the surface-bound $*CO_2$ species. These species are then transformed into $*HOCO$ by reacting with the activated hydrogen species. Then, $*HOCO$ is dissociated into $*OH$ and $*CO$, which are further hydrogenated into $*H_2O$ and $*CH_2$, respectively. Following a series of reactions involving carbon chain growth and hydrogenation, $*CH_2$ is converted into paraffins and olefins, as illustrated in Fig. 11A.[4,80] The product distribution is statistically controlled and approximately follows the Anderson–Schulz–Flory (ASF) model, due to the polymerization mechanism occurring on the open surface of the metal-based catalyst with little steric restriction.[81,82] As depicted in Fig. 11B, the molar fraction (M_n) of a hydrocarbon product with a carbon chain length of n depends on the chain-growth probability (α), as shown in eqn (6), according to the ideal ASF model:

$$M_n = (1 - \alpha)\,\alpha^{n-1} \tag{6}$$

wherein α is determined by the rates of chain propagation (r_p) and chain termination (r_t), as shown in eqn (7):

$$\alpha = r_p/(r_p + r_t) \tag{7}$$

Based on the ASF model, the carbon chain length distribution of the product can be modulated within a certain range by adjusting the chain-growth probability α of the catalyst (Fig. 11C).[80] However, there exist inherent theoretical limits. For example, the selectivity to C_2–C_4 hydrocarbons can hardly exceed 58%, and basically no aromatic hydrocarbons are generated.[83,84] Upon integration with zeolites, not only the carbon chain length distribution can be altered, but aromatics can also be formed through reactions of C–C cleavage of heavy

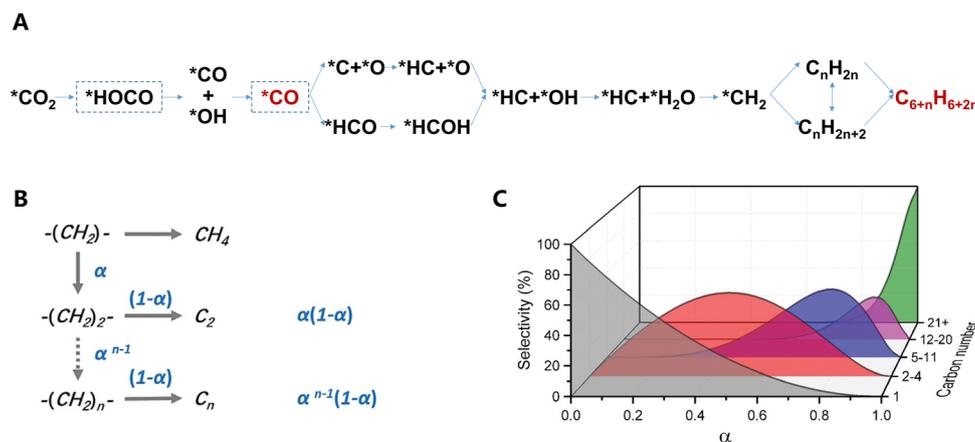Fig. 11 (A) Reaction pathways for CO_2-to-aromatics via the modified Fischer–Tropsch synthesis route. (B) Chain-growth probability α. (C) Regulating the carbon chain length distribution of products by chain-growth probability α. Reprinted and reproduced with permission from Wang et al. Copyright (2021), Elsevier Inc.,[4] and Zhou et al. Copyright (2019), The Royal Society of Chemistry.[80]

hydrocarbons, olefin oligomerization, hydrogen transfer or dehydrogenation, and cyclization (Fig. 4).

3.2. Metal-based materials/zeolite bifunctional catalysts

3.2.1. Metal-based catalysts. The metal-based catalysts utilized in the modified Fischer–Tropsch synthesis route, including metals, metal oxides, or metal carbides, must exhibit multifunctions, including the RWGS reaction, CO/H_2 adsorption and hydrogenation, as well as carbon chain growth. Among the various Fischer–Tropsch synthesis catalysts, such as Fe, Co, Ru and their oxides or carbides, the Fe-based catalyst has demonstrated superior performance in the CO_2-to-aromatics reaction.[37,49] During the CO_2 hydrogenation reaction, the Fe-based catalyst undergoes structural evolution and generates two types of active sites namely Fe_3O_4 and Fe_xC_y (e.g. Fe_5C_2) (Fig. 12A–G).[85] These active sites are responsible for the RWGS and FTS activities, respectively

Fig. 12 (A)–(C) High-angle annular dark-field-scanning transmission electron microscopy (HAADF-STEM) images, (D)–(F) EELS elemental distribution of Fe-xh catalysts, and (G) schematic diagrams of the evolved microstructure of the Fe-based catalyst under the reaction atmosphere of Fischer–Tropsch synthesis. Scale bar, 10 nm. Reprinted with permission from Zhu et al. Copyright (2022), The Authors.[85] (H) RWGS-FTS tandem reaction path over the Fe_3O_4 and χ-Fe_5C_2 sites. Reprinted with permission from Yao et al. Copyright (2020), The Authors.[86]

(Fig. 12H).[86,87] By further conversion of the FTS product over ZSM-5, the product distribution can be adjusted to a larger extent, resulting in an increased proportion of aromatics. However, the C_{5+} product contains a significant amount of gasoline fractions, such as isoparaffins and cycloalkanes, which is attributed to the polymerization mechanism. In light of this, researchers have employed various strategies, including alkali metal modification and introducing a second metal with hydrogenation activity. These strategies enable the adjustment of composition of the active phase and activity for hydrogenation and chain growth for the Fe-based catalysts, therefore optimizing the catalytic performance as summarized in Table 2.

Adjusting the electronic and adsorption properties by alkali metal modification. The adsorption of CO_2 on the Fe-based catalyst involves electron transfer from the catalyst to CO_2. The electron-donating capabilities of alkali metals strengthen the Fe–C chemical bond between CO_2 and the active site, thereby promoting the adsorption of CO_2 molecules, while the adsorption of the electron-donating molecules, such as H_2 and olefin, is weakened. Xu et al. studied the modification of the Fe-based catalysts by Na. In the Na/Fe system, Na acts as an electron donor and creates an environment with a high C^*/H^* ratio on the catalyst surface, which favors the formation and desorption of olefin molecules. Utilizing the bifunctional catalyst consisting of Na/Fe and ZSM-5, the aromatic selectivity reaches approximately 50%, accounting for 94% of the C_{5+} product.[88] Wang et al. synthesized highly dispersed Fe_3O_4 nanoparticles encapsulated in a graphene-like carbon layer by the pyrolysis of Fe-based metal–organic frameworks (Fe-MOFs), taking advantage of the periodic structured frameworks.[89] The Na–Fe@C catalyst was synthesized by further impregnation with Na_2CO_3, which facilitates the formation of olefins due to the high accessibility of active sites and the precise construction of the catalytic interface (Fig. 13A–D). In addition to Na, K is also adopted to modify Fe-base Fischer–Tropsch synthesis catalysts. Ramirez et al. integrated KO_2-doped Fe_2O_3 with ZSM-5 and obtained a 61.4% aromatic fraction in the C_{5+} liquid product in the CO_2-to-aromatics reaction.[92]

Transition metal modification. Song et al. revealed that the modification of a Fe-based catalyst by Cu not only enhances the RWGS activity, but also promotes the stepwise reduction of Fe_2O_3 to Fe_3O_4 and subsequently to α-Fe and facilitates the formation of surface oxygen vacancies in the CO atmosphere. The synergy between Cu and Fe favors the activation and dissociation of H_2, CO_2 and CO, endowing the Cu–Fe_2O_3/HZSM-5 bifunctional catalyst with a superior performance in the CO_2 hydrogenation reaction.[93] Specifically, it achieves a high CO_2 conversion of 56.61%, along with a low CO selectivity of 3.51%, and an aromatic selectivity as high as 61.9%. Cheng et al. discovered the reconstruction of defafossite-$CuFeO_2$ under the reduction and reaction conditions of CO_2 hydrogenation, which led to the formation of Cu, Fe_3O_4 and Fe_5C_2 phases.[37] Among these active phases, Cu plays a pivotal role in promoting the reduction of Fe and enhancing CO_2 adsorption, as well as facilitating olefin desorption. The integration of
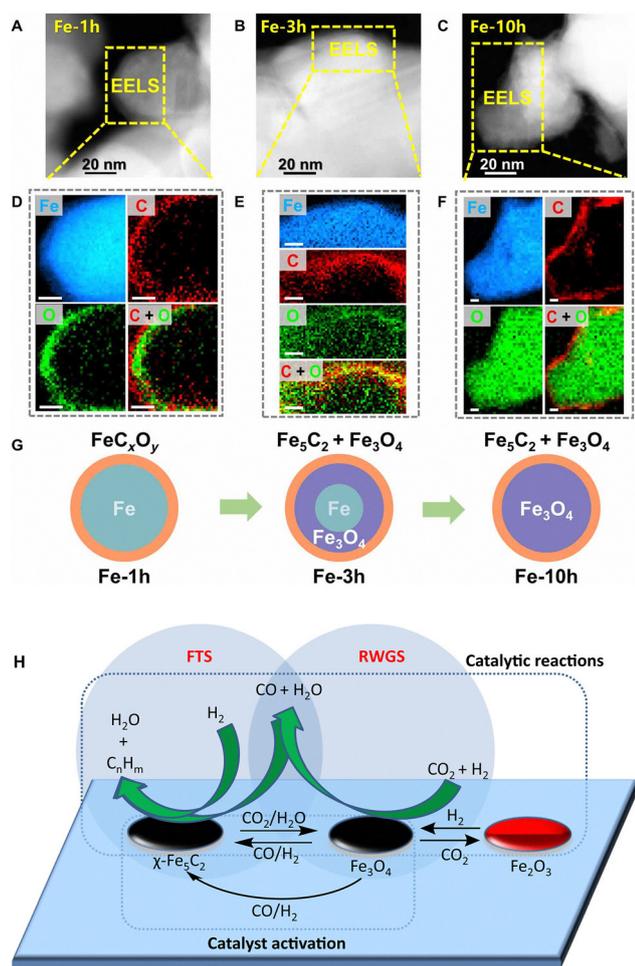
Table 2 CO_2-to-aromatics conversion performance of metal-based materials/zeolites through the modified Fischer–Tropsch synthesis pathway

Catalyst	Temperature (°C)	Pressure (MPa)	Feedstock	Space velocity (mL g^{-1} h^{-1})	CO_2 conv. (%)	CO Sel. (%)	Aro. Sel. (%)	Aro. STY (mmol C g^{-1} h^{-1})	Ref.
Na/Fe/HZSM-5	320	1	$H_2/CO_2 = 3$	2400	29.4	23.1	54.3	3.29	88
Na–Fe/ZSM-5	320	3	$H_2/CO_2/Ar = 71.8/24.3/3.9$	—	33.3	13.3	50.2	—	89
Na–Fe@C/Z-5-ellipsoid	320	3	$H_2/CO_2/Ar = 71.8/24.3/3.9$	9000	34.3	~12	49.6	~14.62	90
NaFe/ZSM-5	320	3	$H_2/CO_2 = 2$	4000	27.7	16	45	6.23	91
Fe_2O_3@KO_2/ZSM-5	375	3	$H_2/CO_2 = 3$	5000	49.8	12.8	24.9	6.03	92
$CuFeO_2$/0.15M-HZSM-5	320	3	$H_2/CO_2 = 3$	8100	52.8	7.3	69.7	30.84	37
6.25Cu–Fe_2O_3/HZSM-5-c	320	3	$H_2/CO_2/N_2 = 72/24/4$	1000	57.3	3.51	56.61	3.35	93
6.25Cu–Fe_2O_3/HZSM-5-pt	320	3	$H_2/CO_2/N_2 = 72/24/4$	1000	55.38	4.41	61.94	3.51	93
$FeMnO_x$/HZSM-5	320	3	$H_2/CO_2/N_2 = 72/24/4$	1000	44.49	11.81	64.24	2.70	94
2.3Na–Cu–Fe_2O_3/HR-Z5-S	320	3	$H_2/CO_2/N_2 = 72/24/4$	1000	33.26	16.03	68.8	2.06	95
3-NFC-5(NaCuFe)/HZSM-5	320	3	$H_2/CO_2/N_2 = 72/24/4$	1500	42.11	~10	50.68	~3.09	96
NFC-DM (NaCuFe)/0.5 -HZSM-5	320	3	$H_2/CO_2/N_2 = 72/24/4$	1500	46.2	6.5	56.1	3.89	97
NaFeMn/core–shell HZSM-5@Si	320	3	$H_2/CO_2/N_2 = 72/24/4$	3000	45	11	64	8.24	98
NaFeMn/ZSM-5	320	3	$H_2/CO_2/N_2 = 72/24/4$	3000	44.49	11.81	56.65	7.14	99
$ZnFeO_x$–4.25Na/S-HZSM-5	320	3	$H_2/CO_2/N_2 = 73/24/3$	1000	41.2	6.9	75.6	3.11	49
NaZnFe/ZSM-5	320	3	$H_2/CO_2/N_2 = 72/24/4$	1000	42.08	<10	63.68	<2.58	100
Na–$FeAlO_x$/Zn–HZSM-5@SiO_2	370	3.5	$H_2/CO_2 = 3$	4000	45.2	—	38.7	—	101
$LaFeO_3$/ZSM-5[a]	350	3	$H_2/CO_2 = 3$	1000	61.2	12	85.8	5.16	102

[a] C–C coupling inhibited on the carburization-resistant $LaFeO_3$ perovskite.

defafossite-$CuFeO_2$ with hierarchical ZSM-5 achieves a high space-time yield of aromatics up to 431.8 mg$_{CH2}$ g$_{cat}^{-1}$ h^{-1}, while the total selectivity to CO and methane is as low as 12%.

The co-modification by alkali metals and transition metals. The co-modification of transition metals, including Zn, Cu, and Mn, with alkali metals can further improve the catalytic performance. Cui *et al.* designed a bifunctional catalyst comprising a Na-modified $ZnFeO_x$ spinel and hierarchical nanocrystalline HZSM-5 zeolite.[49] During pretreatment, the $ZnFeO_x$ phase undergoes reduction to Fe_3O_4, FeO, and α-Fe, which subsequently transform into Fe_3O_4 and Fe_5C_2 under the reaction atmosphere (Fig. 13E and F). Therefore, the coupling of RWGS and FTS is realized. The spinel structure exhibits effective inhibition of nanoparticle sintering. Additionally, the electron-donating properties of Na not only promote CO_2 adsorption and CO conversion, but also inhibit the production of CH_4. It can also modulate the reducibility of $ZnFeO_x$ and optimize the active site composition of Fe_3O_4 and Fe_5C_2. The catalyst achieves a CO_2 conversion of 41.2% and an aromatic selectivity of 75.6%, with the total selectivity to CH_4 and CO below 20%. Yang *et al.* and Chen *et al.* independently investigated the synergistic effects of Cu and Na co-modification.[95,96] They revealed that Na not only promotes the adsorption of CO_2, but also acts as an RWGS active site and enhances the formation of the COOH* intermediates and subsequent CO production. Additionally, Na boosts the carburization process and the formation of Fe carbide species. The adsorption and activation of H_2, along with the H-spillover effect imparted by Cu, enhances the reduction of ferrite species and the formation of oxygen vacancies. This, in turn, promotes the formation of the COOH* intermediate and the non-dissociative adsorption of CO. Additionally, the hydrogen activation and H-spillover effect of Cu can be partially attenuated by Na, which prevents the deep hydrogenation of intermediates and products. Similar co-modification of Na and Mn has also been reported for the NaMn–

Fe catalyst.[94,98,99] Mn increases the tolerance to the poisoning of zeolite by Na and inhibits the coking deactivation by promoting the oxidation of carbon deposition species with CO_2, thus significantly prolonging the catalyst lifetime.[99] By adjusting the spatial arrangement between Na and $FeMnO_x$, the electronic properties of Fe species can be altered, as well as the distribution of the Fe_3O_4 and Fe_5C_2 species, thus remarkably influencing the catalytic performance.[94] The modification of Fe-based FTS catalysts with alkali metals or transition metals enhances the aromatic selectivity, which however cannot exceed 55% and 70%, respectively (Table 2). The co-modification employing both alkali metals and transition metals exhibits greater potential, achieving a significant enhancement in aromatic selectivity up to 75.6%.

Carburization-resistant $LaFeO_3$ perovskite inhibiting uncontrolled C–C coupling. The uncontrollable carbon chain growth on the Fe carbide sites is the determining factor for the low aromatic selectivity of the Fe-based/zeolite catalyst employed in the modified Fischer–Tropsch synthesis pathway. Regarding this, Tian *et al.* designed a $LaFeO_3$ perovskite catalyst. The significant gap between the required migration Fe–Fe distance (2.6–2.8 Å) during phase transition and the actual Fe–Fe distance in the Fe-based perovskite structure (>3.7 Å and >3.90 Å for $LaFeO_3$) makes the carburization of Fe species challenging in such a structure. Furthermore, the A-site cation (La) acts as the pillar anchoring the perovskite $[FeO_6]$ framework. Moreover, the unique empty 4f orbitals of La further enhance the stability of the $[FeO_6]$ framework through a crystal field effect, raising the energy required and suppressing the formation of Fe_5C_2. Consequently, the hydrogenation activity of Fe oxides is fully utilized while eliminating the undesired carbon chain growth activity originating from the Fe carbide species, leading to a breakthrough in the catalytic performance of $LaFeO_3$/ZSM-5 in the CO_2-to-aromatics reaction (Fig. 14).[102] Owing to the absence of Fe carbide sites and consequently the limited C–C
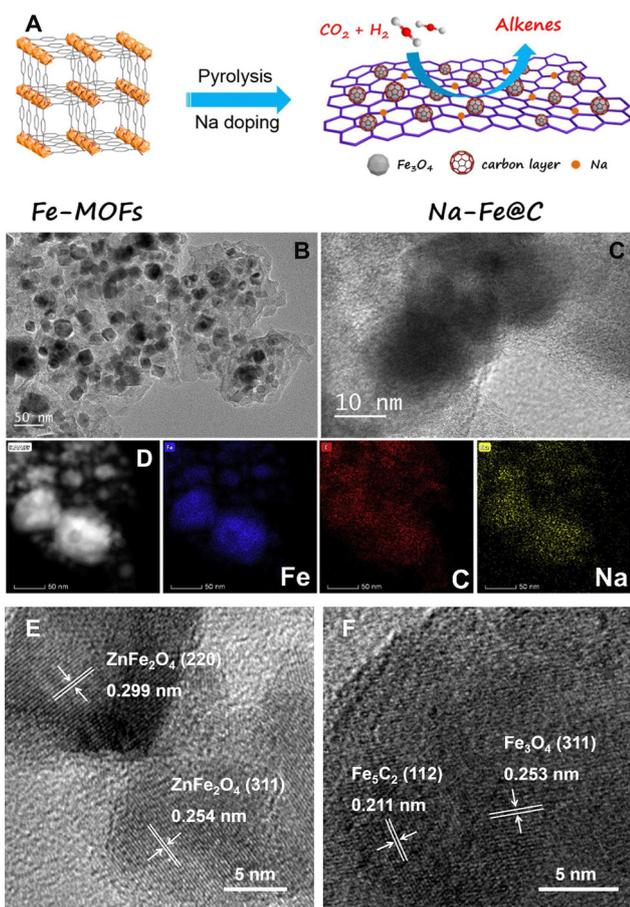
Fig. 13 (A) Preparation of Na–Fe@C by the pyrolysis of Fe-based metal–organic frameworks (Fe-MOFs). (B) TEM and (C) high resolution TEM (HRTEM) images of the used Na-Fe@C catalyst. (D) STEM image of the used Na-Fe@C catalyst and the corresponding elemental mapping of Fe, C, and Na elements. Reprinted with permission from Wang *et al.* Copyright (2020), Elsevier B.V.[89] HRTEM images of Na modified $ZnFeO_x$ (E) after calcination and (F) after reaction. Reprinted with permission from Cui *et al.* Copyright (2019), American Chemical Society.[49]

coupling ability, pure $LaFeO_3$ primarily produces methane in the CO_2 hydrogenation reaction, exhibiting a higher activity compared to Fe_2O_3 or $ZnFe_2O_4$. Upon coupling with ZSM-5, $LaFeO_3$/ZSM-5 achieves an aromatic selectivity of up to 85.8% at a CO_2 conversion of 61.2%, with $HCOOH/H_2CO$ species formed in the RWGS reaction on the Fe oxide as the key intermediates, evidenced by theoretical calculations and experimental results. In conclusion, by designing the $LaFeO_3$ perovskite as a carburization-resistant Fe-based oxide capable of inhibiting carbon chain growth, isolating CO_2 hydrogenation from C–C coupling in the tandem reaction system, and introducing the driving force by the zeolite to redirect the reaction pathway from methane-terminated to aromatic-terminated, a breakthrough in the aromatic selectivity of the Fe-based/zeolite catalyst is finally accomplished.

3.2.2. Zeolite catalysts. Given the partial overlap in the pathways of the CO_2-to-aromatics reaction through the modified Fischer–Tropsch route and the methanol-mediated route, studies are similarly concentrated on altering the acidic

properties and pore structure of zeolites, as well as the positioning of acid sites.

The morphology and pore structure. Compared with the methanol-mediated route, the modified Fischer–Tropsch route suffers from more significant coking deactivation, attributed to the considerable long-chain products generated by the Fischer–Tropsch synthesis reaction. Strategies aimed at improving diffusion efficiency through optimizing the morphology and pore structure of zeolite have been proposed.[37,49,89,95,100] Cui *et al.* synthesized a nanocrystalline ZSM-5 (Fig. 15A and B), which is characterized by a hierarchical pore structure and suitable acidity, thereby facilitating the diffusion of olefins and aromatics, and consequently enhancing catalytic activity while inhibiting coke deposition.[49] Wang *et al.* processed the parent ZSM-5 crystals using NaOH solutions of varying concentrations to create hollow-structured ZSM-5.[89] Utilizing the local desilication etching induced by the radial gradient of framework aluminum, desilication is suppressed on the Al-rich surface while being promoted in the Al-poor bulk. The sample exposed to 0.2 M NaOH solution, denoted as H-ZSM-5-0.2 M, demonstrates a hollow structure comprising a thin shell of approximately 20 nm (Fig. 15C and D), featuring mesopores with a diameter of approximately 10 nm. This unique structure enhances mass transfer during the catalytic reaction and improves the reaction efficiency compared with the original ZSM-5. Jiang *et al.* incorporated polyethylene glycol (PEG) as a porogen during the synthesis of ZSM-5 leveraging the encapsulation effect of PEG within the crystallization system.[100] They realized the construction of intracrystalline mesopores with a diameter of 4–10 nm and the weakening of strong acid sites, thereby promoting the generation and diffusion of aromatics.

The properties and positioning of acid sites. Wei *et al.* explored the influence of Brønsted acidity on the formation of aromatics and coke deposition in the CO_2-to-aromatics reaction, by combining a series of ZSM-5 zeolites with diverse Brønsted acidities with a NaFe catalyst.[91] The study demonstrates that an increase in Brønsted acid density is beneficial for the aromatization of olefins, whereas an excessive number of Brønsted acid sites may accelerate coke deposition and catalyst deactivation. The impregnation of $(NH_4)_2HPO_3$ with an appropriate amount of phosphorus can effectively reduce the Brønsted acid density and improve the aromatic selectivity.[94] Regarding the side reactions, such as alkylation and isomerization, occurring on the external acid sites, various studies have reported the passivation of these sites by chemical liquid deposition of SiO_2 (Fig. 16A)[49,88,91] and coating with a silicalite-1 shell.[37,98] For example, after the silanization treatment, the NaFe/ZSM-5 catalyst achieves a 75% proportion of light aromatics in overall aromatics and with a 72% *para*-xylene/xylene (PX/X) fraction.[91] Similarly, the PX/X fraction reaches 75% and 66.9% in the Na–$ZnFeO_x$/ZSM-5[49] and $CuFeO_2$/ZSM-5[37] catalytic systems, respectively. Gu *et al.* synthesized ZSM-5 zeolites with varying aluminum positioning and acid properties by altering the raw
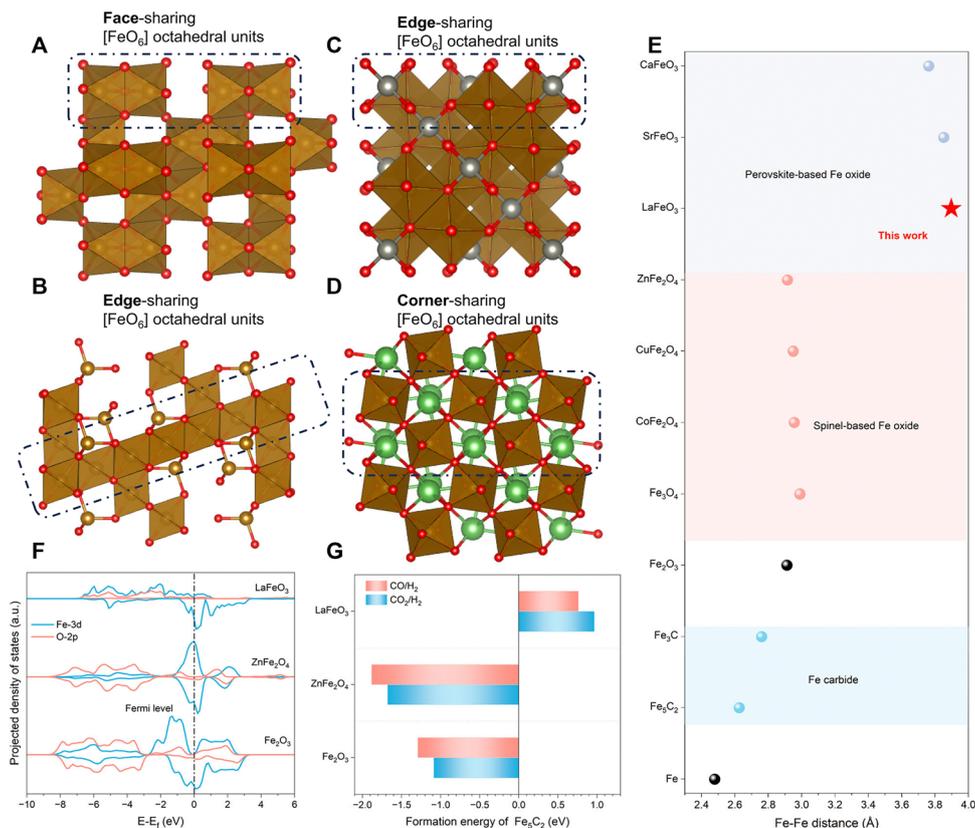
Fig. 14 The design of the LaFeO₃ perovskite as a carburization-resistant Fe-based oxide. Atomic structural model of (A) Fe_2O_3, (B) Fe_3O_4, (C) $ZnFe_2O_4$, and (D) $LaFeO_3$, showing different connection modes of [FeO₆] octahedra. Spheres in red, brown, silver, and green represent O, Fe, Zn, and La atoms, respectively. (E) Fe–Fe distances of Fe, Fe carbides, and various Fe oxides. (F) Projected density of states (PDOSs) of Fe_2O_3, $LaFeO_3$, and $ZnFe_2O_4$. (G) Calculated formation energies of per mole Fe_5C_2 through the reduction of Fe_2O_3, $ZnFe_2O_4$ and $LaFeO_3$ by typical reactive atmospheres. Reprinted with permission from Tian et al. Copyright (2024), The Authors.[102]
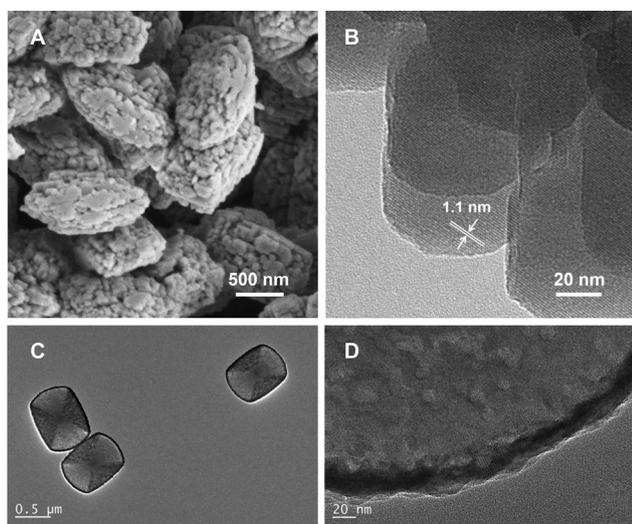
materials and synthesis methods and subsequently applied them in the CO₂-to-aromatics reaction in combination with

Fig. 15 (A) and (B) The nanocrystalline ZSM-5 with hierarchical pore structure. Reprinted with permission from Cui et al. Copyright (2019), American Chemical Society.[49] (C) and (D) hollow-structured ZSM-5 for the CO₂-to-aromatics reaction. Reprinted with permission from Wang et al. Copyright (2020), Elsevier B.V.[89]

Na–Fe@C.[90] Consequently, the relationship between aluminum positioning and product distribution was elucidated through detailed characterization and theoretical calculation. The aluminum species located within the straight and sinusoidal channels tend to catalyze the cracking or isomerization reactions of the intermediates due to steric hindrance, while those situated at the intersection of 10-MR pore channels facilitate the aromatic formation due to the low energy barrier of the aromatization reaction (Fig. 16B and C).

4. Several novel coupling routes of CO₂-to-aromatics

4.1. CO₂ hydrogenation coupled with CO hydrogenation

RWGS is one of the principal side reactions in the CO₂-to-aromatics reaction system. Despite the possibility of recycling the by-product CO for further conversion, its generation significantly reduces the carbon conversion efficiency in a single pass. Given that RWGS is a reversible reaction between CO₂ and CO, the introduction of CO into the feedstock will shift the reaction equilibrium according to the Le Chatelier principle. Moreover, taking advantage of the similarity in the activation and conversion of CO₂ and CO, the coupling of CO₂ hydrogenation and CO
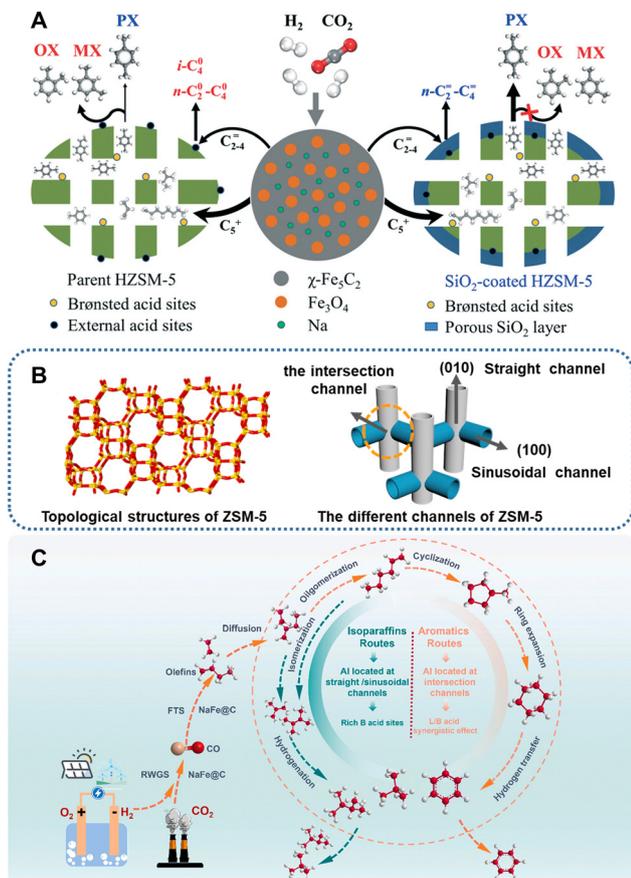
Fig. 16 (A) Scheme of the xylene isomerization reaction on ZSM-5 with and without the modification of SiO$_2$. Reprinted with permission from Xu et al. Copyright (2019), The Royal Society of Chemistry.[88] (B) Topological structure and the corresponding channels of ZSM-5, and (C) the reaction pathway and product distribution at different aluminum positionings. Reprinted with permission from Gu et al. Copyright (2024), Elsevier B.V.[90]

Fig. 17 The coupling of CO$_2$ hydrogenation with CO hydrogenation. (A) 667 mg of ZnAlO$_x$&H-ZSM-5, 320 °C, 3.0 MPa, H$_2$/CO$_2$/Ar = 3/1/0.2, 66.7 mL min^{-1}, CO = 0–26.6 mL min^{-1}. Reprinted with permission from Ni et al. Copyright (2018), The Authors.[41] (B) 0.25 g of Cr$_2$O$_3$ or 0.5 g of Cr$_2$O$_3$/H-ZSM-5, 350 °C, 3 MPa, H$_2$/CO$_2$ = 3 (5.42 vol% CO), 10 mL min^{-1}, * refers to the results without CO. Reprinted with permission from Wang et al. Copyright (2019), American Chemical Society.[55]

hydrogenation reactions has the potential to improve the overall reaction efficiency.

In an investigation focusing on the methanol-mediated pathway, Ni et al. compared the reaction performance of ZnAlO$_x$/ZSM-5 at different CO/CO$_2$ feed ratios. The introduction of CO has little effect on the aromatic selectivity, but it markedly reduces the CO selectivity to a minimum of 12.6% at a CO/CO$_2$ ratio of 1.8/1 (Fig. 17A).[41] According to Wang et al., the Cr$_2$O$_3$/ZSM-5 bifunctional catalyst exhibits a CO selectivity of 41.2% when fed with pure CO$_2$ and H$_2$. Upon adding 5.42% CO to the feedstock, the CO selectivity decreases drastically to 11.4%, indicating a higher conversion efficiency of CO$_2$ to form high-value organic products (Fig. 17B).[55] Similar results have also been reported for the modified Fischer–Tropsch pathway. For example, Ramirez et al. introduced an equivalent amount of CO into the CO$_2$ hydrogenation system (a CO/CO$_2$ ratio of 1) catalyzed by Fe$_2$O$_3$@KO$_2$/ZSM-5.[92] At the constant H$_2$/(CO + CO$_2$) ratio of 3, the CO$_x$ conversion increases from 48.9% in the pure CO$_2$ system to 58.4% in the CO/CO$_2$ mixed system, along with the increased aromatic selectivity from 24.9% to 28.4%.
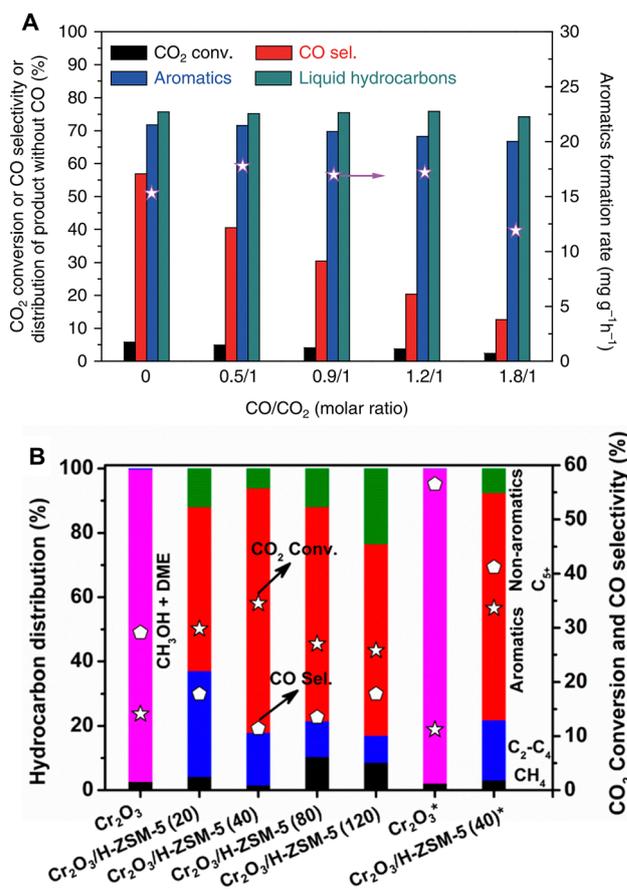
4.2. CO$_2$ hydrogenation coupled with aromatic alkylation

Zuo et al. employed the ZnZrO$_x$/ZSM-5 catalyst for the coupling reaction of CO$_2$ hydrogenation and toluene methylation.[103] In the conventional toluene methylation reaction using methanol as the methylation reagent, the conversion of methanol into surface methoxy species is the rate-determining step. By coupling the toluene methylation reaction with the CO$_2$ hydrogenation reaction, CO$_2$ is first hydrogenated on the ZnZrO$_x$ surface via the formate path, generating methoxy species that subsequently migrate to the pore structure of ZSM-5 and undergo Friedel–Crafts methylation with toluene as the methylation agent (Fig. 18A). Compared with the methylation of toluene by methanol, the activation energy decreases from 108.5 ± 3.6 kJ mol^{-1} to 83.2 ± 1.5 kJ mol^{-1} upon coupling with the CO$_2$ hydrogenation reaction. Furthermore, the para-selectivity of xylene increases from 32.7% to 70.8% due to the dynamic equilibrium between the generation and consumption of methoxy species, thereby preventing side reactions such as deep methylation and methanol to hydrocarbon (MTH) conversion resulting from the accumulation of methoxy species.
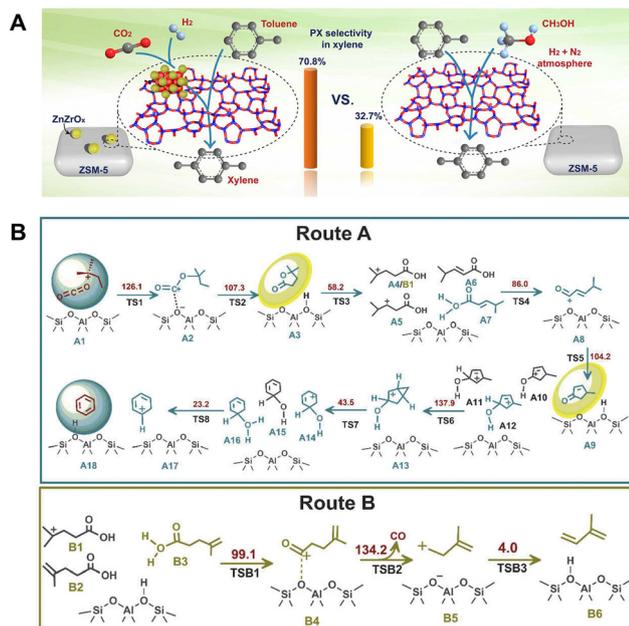
Fig. 18 (A) Comparison of the performance of toluene methylation with methanol or by coupling the CO_2 hydrogenation reaction. Reprinted with permission from Zuo *et al.* Copyright (2020), The Authors.[103] (B) The proposed mechanism of *n*-butane aromatization coupled with CO_2 over ZSM-5. Route A: formation of aromatics; Route B: formation of CO. The calculated free energy barriers of all the elementary reactions (at 450 °C) are given in kJ mol^{-1}. Reprinted with permission from Wei *et al.* Copyright (2023), Dalian Institute of Chemical Physics, the Chinese Academy of Science.[107]

To align the temperature window of the CO_2 hydrogenation and methylation reactions, this team modified ZnZrO$_x$ with Cu to enhance its activity and decrease the reaction temperature. The CuZnZrO$_x$/ZSM-5 catalyst facilitates the selective synthesis of durene by coupling the CO_2 hydrogenation reaction with the methylation of trimethylbenzene.[104] Cao *et al.* further developed a ZnZrO$_x$/Al$_2$O$_3$/ZSM-5 triple composite catalyst based on ZnZrO$_x$/ZSM-5. In this catalytic system, methanol generated from CO_2 hydrogenation over ZnZrO$_x$ is dehydrated at the Lewis acid site of Al$_2$O$_3$ to form dimethyl ether, which then reacts with benzene to produce toluene and xylene.[105] Miao *et al.* also achieved the coupling of CO_2 hydrogenation with toluene methylation in the ZnCrO$_x$/ZSM-5 catalytic system.[106] Through optimal combination (particle mixing), the moderate proximity between the catalytic components promotes the methylation of toluene while inhibiting deep methylation, thereby improving the xylene selectivity. By further modification of ZSM-5 with P and silica, an 82.8% *para*-xylene fraction in xylene and a 75.8% light olefin fraction in aliphatic hydrocarbons are achieved at a CO_2 conversion of 20.9% and toluene conversion of 10.6%.

In the aforementioned studies, the methylation of aromatics with CO_2 as the methoxy source has been realized by coupling the reactions of CO_2 hydrogenation and aromatic methylation. Nonetheless, as the methylation reaction is prior to the side chain growth reaction, the substituents primarily consist of methyl groups, posing challenges in producing compounds with long-chain substituents, such as ethylbenzene or propylene. With respect to this, Zuo *et al.* established a tandem coupling reaction route consisting of "CO_2 hydrogenation to light olefins" and "alkylation of benzene with light olefins".[108] In a dual-bed catalytic system comprising ZnZrO$_x$/SAPO-34 and ZSM-5, CO_2 is initially converted into ethylene or propylene through the upper bed of ZnZrO$_x$/SAPO-34, and subsequently, the ethylene/propylene diffuses to the lower bed of ZSM-5 and reacts with benzene to form ethylbenzene or propylene. Phosphorus modification was employed to tune the medium-strong acidity of ZSM-5, thereby inhibiting the deep hydrogenation of olefins and optimizing the distribution of aromatics. The product distribution gradually shifts from ethylbenzene to propylene with the increase of phosphorus content. Consequently, the sequential construction of side chain groups and their substitution onto benzene is efficiently coupled, achieving selectivities of 83.5% and 64.7% for ethylbenzene and propylene, respectively, within the overall aromatics.

4.3. CO_2 hydrogenation coupled with alkane aromatization

Introducing CO_2 into the aromatization of hydrocarbons is another alternative coupling reaction pathway, in which CO_2 is used as the carbon source for aromatic synthesis. Bu *et al.* developed a catalyst for the coupling of CO_2 and propane aromatization.[109] By incorporating Ga into the MFI framework to create medium-strength Brønsted acid sites, the dehydrogenation of propane is favored, while the cleavage of C–C bonds is suppressed. Simultaneously, Cu was introduced to obtain a suitable Lewis-Brønsted acid distribution, thus enhancing the adsorption and conversion of CO_2 and facilitating the consumption of hydrogen species generated during alkane aromatization. The resultant Cu/Ga-MFI catalyst exhibits a 93.6% propane conversion and 73% aromatic selectivity.

Wei *et al.* developed the coupling strategy involving CO_2 hydrogenation and alkane aromatization, which is applicable for a broader spectrum of alkanes.[107] By introducing CO_2 into the ZSM-5-catalyzed aromatization of *n*-butane, *n*-pentane, and *n*-hexane, the production of methane, ethane, and propane is inhibited, resulting in aromatic selectivity exceeding 80%. This unusually high aromatic selectivity is beyond the theoretical limit ($\sim$50%) for alkane aromatization *via* the hydrogen transfer pathway in the absence of CO_2, suggesting that the CO_2 molecules are involved in the reaction. The underlying mechanism was clarified by GC-MS analysis of the dissolved carbon species within consumed zeolite, *in situ* characterization, and density functional theory (DFT) calculations. In the coupling reaction system, carbonium ions generated from alkane cracking are inserted by CO_2 to form alkyl carbonate species, which are further cyclized into methyl-substituted lactones (MLTOs) and then converted into methyl-substituted cycloalkenones (MCEOs). The MLTOs and MCEOs are identified as the key intermediates in this reaction, with 25% of CO_2 incorporated into the aromatic products (Fig. 18B).

Research has also been conducted on the catalytic conversion of polyolefin and CO_2. Chen *et al.* proposed a novel catalytic reaction pathway utilizing Cu–Fe$_3$O$_4$ and Zn/ZSM-5,

which enables the simultaneous conversion of polyethylene and CO_2 into aromatics and CO.[110] In this reaction, CO_2 is converted into CO through the RWGS reaction, which is hydrogen consuming, thereby suppressing the hydrogen transfer reaction, preventing the resulting formation of alkanes, and promoting the selective formation of aromatics with a maximum selectivity of 64.0%.

5. Rational design of multi-functional catalysts and optimizing the coupling catalytic route for CO_2-to-aromatics reactions

The direct conversion of CO_2 into aromatics can be realized through diverse coupling catalytic routes. Taking the methanol-mediated pathway and the modified Fischer–Tropsch synthesis route as an example, CO_2 undergoes direct conversion to methanol over the metal-based catalyst or is transformed into methanol or olefins via the RWGS reaction, followed by hydrogenation or chain growth. The aromatic products with specific distribution are generated through the aromatization and alkylation of methanol or olefins over the zeolite-based catalyst. By introducing CO, alkanes, or aromatics at different reaction steps, new coupling routes are constructed, which generally adhere to the similar reaction path (Fig. 19). All aforementioned coupling catalytic strategies rely on the matching and synergy between the metal-based catalysts (metal, metal oxide, or metal carbide) and zeolites.

The activation and hydrogenation of CO_2 is the primary reaction step in various coupling systems. As illustrated in Fig. 19, the RWGS reaction occurs across different systems, resulting in a considerable CO selectivity in the final product despite subsequent CO transformation. Notably, the CO–CO_2 interconversion is common over metal-based catalysts. For instance, in the CO-to-aromatics reaction via the methanol-mediate pathway, CO_2 emerges as the dominant byproduct due to the Boudouard or water-gas shift (WGS) reactions, with 40–50% selectivity.[8] Consequently, CO and CO_2 hydrogenation to aromatics exhibits comparable reaction mechanisms and catalytic

system compositions. For example, the active elements are both selected from Zn, In, Cr, Zr, etc., for the methanol-mediated route, or Fe for the modified Fischer–Tropsch synthesis route. However, the CO and CO_2 conversion reactions exhibit fundamental distinctions, primarily originating from the difference in C–O bond characteristics. The corresponding metal-based catalysts are different in composition, for example, the Zn–Zr binary oxide exhibits an optimal Zn/Zr ratio of 1/200 in the CO-to-aromatics system,[30] compared to the higher ratio in the range of 1/8–1/2 observed in the CO_2-to-aromatics reaction. In addition, the significant generation of H_2O in the CO_2 hydrogenation system imposes higher requirements on the water resistance of the metal-based catalysts. Based on the similarities and existing research findings on the CO- and CO_2-to-aromatics reactions, developing metal-based catalysts with dual CO/CO_2 hydrogenation activity represents a critical strategy to enhance the catalytic efficiency of CO_x-to-aromatics reactions.

Within the multi-functional catalytic system, the zeolite component catalyzes the subsequent transformation of bridging intermediates, which are generated from the metal-based catalyst. Two typical coupling reaction systems, namely the methanol-mediated route and the modified Fischer–Tropsch synthesis pathway, generate methanol and olefins as intermediates, respectively, thereby imposing different demands on the zeolite component. Specifically, the zeolite-catalyzed aromatization and alkylation processes lead to a specific distribution profile of aromatic hydrocarbons in the final product mixture. From the perspective of aromatization, the conversion of both methanol and olefins into aromatics requires the role of Brønsted acid sites, but with different strengths and densities. The ZSM-5 zeolite employed in the modified Fischer–Tropsch synthesis route exhibits a relatively lower Si/Al ratio of 10–80, whereas the methanol-mediate pathway typically demands a higher Si/Al ratio ranging from 40 to 150, with extreme cases up to 600. Furthermore, constructing the synergy between Brønsted and Lewis acidic sites and controlling the framework aluminum distribution within the pore structures are also critical strategies for tuning aromatization processes in these catalytic systems. From the perspective of alkylation, the aromatic distribution can be controlled through morphological engineering of zeolites particularly b-axis length modulation and external acidity modification. While the coupling reaction of CO_2 hydrogenation with aromatic alkylation usually does not involve the formation of new aromatic rings, the shape-selectivity of zeolites remains the determining factor for the distribution of aromatic products.

Beyond the design of metal- and zeolite-based catalytic sites, the matching between these two distinct types of sites is also critical for constructing multi-functional catalysts for the coupling catalytic routes. A series of coupling effects are involved, which need to be systematically optimized and precisely controlled through the rational design of catalysts.

5.1. Coupling effects

The one-step conversion of CO_2 to aromatics is realized through the coupling of diverse reaction routes, linked by the formation, transfer and conversion of intermediate species. A
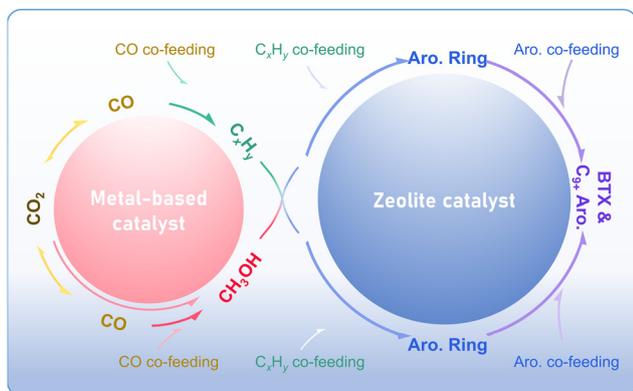

Fig. 19 The coupling catalytic routes for CO_2 conversion to aromatics over multi-functional catalysts.
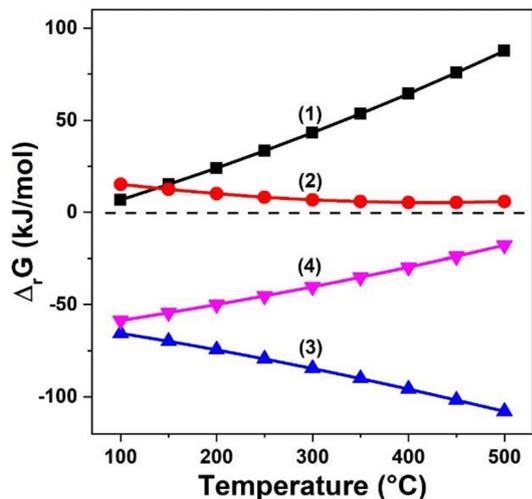
Fig. 20 Calculation of the Gibbs free energy change of: (1) CO_2 hydrogenation to methanol, (2) RWGS, (3) methanol to xylene, and (4) CO_2 hydrogenation to xylene. Reprinted with permission from Li et al. Copyright (2019), Elsevier Inc.[60]

series of coupling effects have been revealed from the aspects of thermodynamics, kinetics and even reaction mechanisms.

Taking the methanol-mediated route as an example, this route necessitates a high temperature above 400 °C due to the substantial activation energy required for the methanol to aromatic (MTA) reaction. Nonetheless, as a strong exothermic reaction, the hydrogenation of CO_2 to methanol is thermodynamically unfavorable at such high temperature. By coupling the MTA and CO_2 hydrogenation reactions, the conversion of CO_2 to aromatics becomes more thermodynamically feasible (Fig. 20).[60] Additionally, according to the Le Chatelier principle, the immediate consumption of methanol through the MTA reaction provides driving force for the CO_2 conversion, which shifts the reaction equilibrium in the direction of aromatic formation.[80] Li et al. compared the activity of ZnZrO and ZnZrO/ZSM-5 in the CO_2 hydrogenation reaction.[60] ZnZrO/ZSM-5 demonstrates significantly higher CO_2 conversion and space–time yield of organic products than ZnZrO, validating that the consecutive reaction of CO_2 to form aromatics is not a simple combination of reaction steps on two kinds of catalytic components, but rather a well-coupled tandem process.

Wang et al. compared the performance of HZSM-5 and Cr_2O_3/H-ZSM-5 in the MTA and CO_2-to-aromatics reactions and proposed the reinforcement effect of CO_2 on aromatization in the tandem reaction system.[54] Two distinct pathways compete for the conversion of olefins in zeolites, namely the deep hydrogenation leading to alkanes and the dehydro-cyclization resulting in aromatics. In the presence of Cr_2O_3 and CO_2, the hydrogen species produced from the dehydrogenation of olefins can be consumed in-situ by reacting with CO_2 under the catalysis of Cr_2O_3. This effectively inhibits the deep hydrogenation of olefins and enhances the formation of aromatics. Similar coupling effects have also been revealed in the $ZnZrO_x$/ZSM-5 catalytic system, wherein the aromatization is promoted by the metal oxide-assisted CO_2 dehydrogenation.

Additionally, in the modified Fischer–Tropsch route, a variety of catalysts, including Na–Fe@C/ZSM-5,[89] Cu–Fe/ZSM-5,[93] and $CuFeO_2$/ZSM-5,[37] have exhibited the coupling effect of the CO_2-assisted dehydrogenation and aromatization. For example, Song et al. proposed a "H Recycling" mechanism, in which hydrogen species resulting from the aromatization reaction diffuse out of the zeolite and are promptly consumed by reacting with CO_2 over the metal oxide, thereby promoting both the CO_2 hydrogenation and aromatization reactions.[93]

5.2. Impact of intimacy or distance on the spatial coordination of catalytic components

The coupling of two catalytic components depends not only on the precise matching of bifunctional activities, but also on the spatial coordination of catalytic sites, which determines the transfer of intermediates between different catalytic sites. Weisz et al. investigated the effect of proximity between bifunctional catalytic components in a series of reactions, such as alkane isomerization and hydrocracking.[111] In reactions involving stable intermediates, a shorter distance between catalytic sites facilitates the transfer of intermediates, and therefore the catalytic performance shows the characteristic of "the closer, the better".

Using the CO_2-to-aromatics reaction system via the methanol-mediated route, Wang et al., Li et al., and Zhou et al. individually evaluated the catalytic performance by employing different combination manners of catalytic components, ranging from powder mixing at the nanometer scale to granule mixing at the micrometer scale and extending to dual-bed packing at the centimeter scale.[55,60,62] Enhanced catalytic activity and aromatic selectivity are observed at a smaller mixing scale (Fig. 21A). Regarding the modified Fischer–Tropsch route, Song et al. also compared the catalytic performance of Cu–Fe/ZSM-5 with different coupling manners, revealing that the short diffusion path between the two components in the granule mixing manner accelerates the transfer and consumption of olefins and therefore promotes the thermodynamic equilibrium shift of the CO_2 conversion reaction.[93] However, further shortening the distance through powder mixing resulted in a decrease in catalytic activity while an increase in methane selectivity (Fig. 21B). Similarly, in other catalytic systems, such as Na–Fe@C/ZSM-5,[89] Na–Cu–Fe_2O_3/ZSM-5,[95] and NaZnFe/ZSM-5,[100] the optimal activity and aromatic selectivity were also achieved at a moderate coupling scale of micrometers through granule mixing.

The influence of intimacy or distance partially originates from the distance-dependent structural stability of the catalytic components. The coupling systems of metals, metal oxides, or metal carbides with zeolites are composed of two types of components with distinct diversity in phase and properties. The intimate physical integration between these two components, along with the harsh reaction conditions of high temperature and the reducing and moist atmosphere, may induce the structural evolution and element migration of the catalyst. Ding et al. investigated the migration behavior of metal species in the $ZnCrO_x$/SAPO-34 catalyst at different coupling scales under the atmosphere of H_2/CO.[115] The Zn species can easily
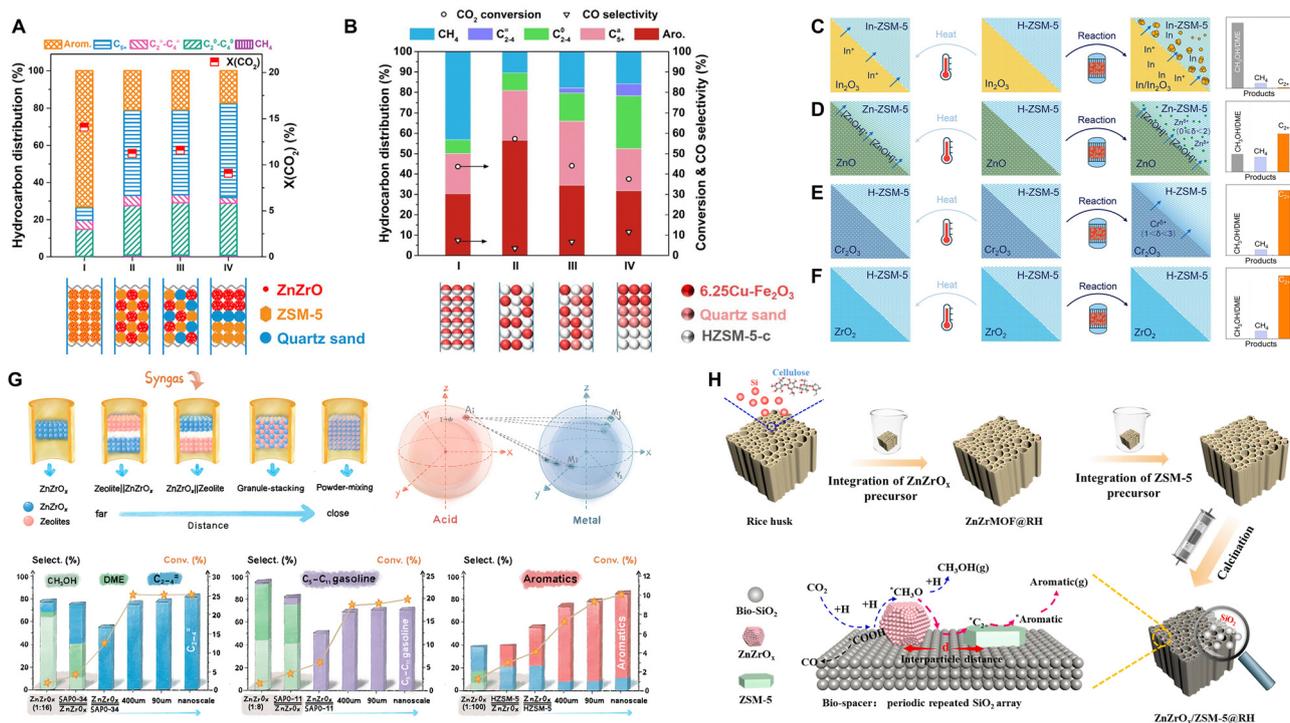
Fig. 21 Effect of the coupling distance scale of bifunctional catalytic components in the CO₂-to-aromatics reaction via (A) the methanol-mediated route and (B) the modified Fischer–Tropsch route. Reaction conditions: (A) ZnZrO/ZSM-5, 320 °C, 4.0 MPa, $H_2/CO_2/Ar$ = 72/24/4, 1200 mL g^{-1} h^{-1}; (B) 6.25Cu–Fe₂O₃/HZSM-5-c, 320 °C, 3.0 MPa, $H_2/CO_2/N_2$ =72/24/4, 1000 mL g^{-1} h^{-1}. Reprinted with permission from Li et al. Copyright (2019), Elsevier Inc.,[60] and Song et al. Copyright (2020), American Chemical Society.[93] The migration of metal species from metal oxides to zeolites driven by high-temperature treatment and reaction and its effect on the CO₂ hydrogenation reaction: (C) In₂O₃/H-ZSM-5, (D) ZnO/H-ZSM-5, (E) Cr₂O₃/H-ZSM-5 and (F) ZrO₂/H-ZSM-5. Reprinted with permission from Wang et al. Copyright (2021), Wiley-VCH GmbH.[112] (G) Dependence of the distance between metal oxides and zeolites for reactions following the simple tandem or synergistic tandem mechanism. Reprinted with permission from Li et al. Copyright (2022), American Chemical Society.[113] (H) Anchoring the metal oxide and zeolite components with the rice husk derived-SiO₂. Reprinted with permission from Li et al. Copyright (2023), Elsevier B.V.[114]

diffuse into SAPO-34 and react with the Brønsted acid sites to form the Zn–OH species under the nanoscale coupling distance. At a smaller scale, the migration can be further enhanced. Wang et al. systematically examined the migration behavior of different metal oxides, including In₂O₃, ZnO, Cr₂O₃, and ZrO₂, in the CO₂ hydrogenation reaction atmosphere.[112] Among the studied metal oxides, In₂O₃, ZnO, and Cr₂O₃ are easily reduced at high temperature, and In and Zn can further migrate to ZSM-5 in the form of In^+ and $[ZnOH]^+$, respectively. The following ion exchange of ZSM-5 by the In^+ and $[ZnOH]^+$ species then leads to the loss of hydrogenation activity of the metal oxides, as well as the deactivation of Brønsted acid sites of zeolites (Fig. 21C–F). Similar metal migration phenomena are more significant in the alkali metal-modified Fe-based catalyst systems, which is the primary cause for the reduced activity of the multi-component catalysts coupled in the powder mixing manner.[89,93,95,100] Ramirez et al. detected the migrating species such as $K(H_2O)^{8+}$ in the KO₂@Fe₂O₃/ZSM-5 system by high-field 39K ssNMR spectroscopy.[92] Cui et al. found that at a coupling distance of hundred-nanometer scale between ZnFeOₓ–Na and ZSM-5, the sodium ions may diffuse from ZnFeOₓ–Na to ZSM-5 and poison the zeolite acid sites, resulting in a severe deactivation of the zeolite component.[49] Based on the high migratability of Cu species, Chen et al. constructed an

extra-framework Al (Al^{EF}) layer by treating ZSM-5 with the $Mn(NO_3)_2$ solution and used these kinds of Lewis acid sites as acceptors for the migrating Cu species. Therefore an RWGS-active region was built on the external surface of the zeolite in the CuNa–Fe/ZSM-5 catalyst, which promotes the CO₂ hydrogenation reaction.[97]

Another underlying key factor in the impact of intimacy or distance is the adsorption–desorption-diffusion behavior of intermediate species. Arslan et al. observed the "asymmetric desorption behavior" of oxygenated hydrocarbon pool species and aromatics in the ZnCrOₓ/ZSM-5-catalyzed CO/CO₂ hydrogenation reaction system.[45] Compared with the bare ZSM-5, the intimate contact between ZnCrOₓ and ZSM-5, particularly at their interface, reduces the desorption energy of aromatic molecules. For example, the desorption energy of para-xylene declines from 85.4 kJ mol^{-1} to 76.9 kJ mol^{-1}. Meanwhile, the desorption energy of oxygenated hydrocarbon pool species, such as aromatic aldehydes or aromatic alcohol, is increased. For example, the desorption energy of phenol rises from 89.05 kJ mol^{-1} to 106.83 kJ mol^{-1}. This asymmetric desorption behavior demonstrates the effect of selective permeabilization, leading to an enrichment of oxygenated hydrocarbon pool species inside the zeolite pores and promoting the diffusion of aromatic products. Hence, it significantly improves the

activity, aromatic selectivity, and stability of the catalyst. Li et al. quantitatively studied the effect of the distance between metal oxides and zeolites within the scale range of nano- to millimeters, in the syngas-to-olefin (STO), gasoline (STG), and aromatic (STA) reaction systems.[113] Using the Peclet number (Pe) to assess the back-mixing degree (i.e. the diffusion range of methanol countercurrently in a fixed-bed reactor, driven by its diffusivity), they proposed the simple tandem and synergistic tandem mechanism. Among the syngas conversion reactions, STO and STG follow the simple tandem mechanism. Provided that the methanol intermediate can swiftly diffuse onto the acid site of zeolites, the catalytic performance remains insensitive to the distance between metal oxides and zeolites. In contrast, the STA reaction follows the synergistic tandem mechanism, where the hydrogen species generated by dehydrogenation of methanol within the zeolite needs to be consumed by oxides to facilitate further aromatic formation. Hence, a close proximity between metal oxides and acid sites of zeolites is essential (Fig. 21G). Li et al. developed a catalyst preparation method to anchor the metal oxide and zeolite components using the rice husk derived-SiO_2.[114] They introduced a dimensionless constant to quantitatively characterize the component coupling scale and emphasized that the intimate contact between oxide and zeolite facilitates the transfer and further transformation of intermediates, such as *HCOO and *CH_3O. Furthermore, the anchoring of metal oxides and zeolites by SiO_2 enhances the catalyst stability in the CO_2-to-aromatics reaction (Fig. 21H). These studies provide valuable insights into the quantitative understanding of the effect of coupling intimacy or distance.

5.3. Constructing the spatio-temporal coupling and directional spatial pathway for tandem reactions

Coupling catalysis is a strategy for achieving a multi-step reaction in a single process through the integration and synergy of multi-functional catalysts. Therefore, in tandem reactions such as CO_2-to-aromatics, coupling catalysis involves spatio-temporal effects, manifesting as a temporal sequence of reactions across a spatial distribution of catalytic sites, with the transfer of intermediate species serving as the key bridge. Diffusion is governed by two crucial parameters: distance and direction. As mentioned hereinbefore, numerous studies have focused on regulating the diffusion distance of intermediate species by modulating the coupling intimacy between catalytic components, which ultimately influences the catalytic performance. However, the diffusion direction has received limited attention. The Xie and Wang group has reported advances in the direct conversion of CO/CO_2 to aromatics based on the coupling catalysis of metal oxides and zeolites.[79,116–118] Focusing on the oriented diffusion of intermediate species within the anisotropic pore structure of zeolites, they unveiled the spatial pathway for the diffusion and transformation of intermediates. Additionally, the directional spatial pathway was constructed by designing an orient-distributed metal oxide/zeolite bifunctional catalyst.

Revealing the spatial pathway for the diffusion and transformation of intermediates based on the spatial anisotropy of the zeolite pore structure. The morphology of zeolites is closely related to their anisotropic diffusion properties and the spatial positioning of acid sites. A series of ZSM-5 zeolites with various morphologies and sizes were synthesized at a constant Si/Al ratio, including the plate-like pZ5-x and ConZ5-y with a conventional elliptic column morphology (Fig. 22A).[79] When employed in the CO_x-to-aromatic reaction, reducing the external acidity of zeolites by increasing its crystal size results in a shift in the aromatic distribution towards C_6–C_8 light aromatics, in agreement with the consensus that C_{9+} aromatics primarily originate from the alkylation of light aromatics on the external acid sites of the ZSM-5 zeolite. However, the morphology of the ZSM-5 zeolite also plays a key role, which had not been well discussed. By decoupling the aromatization and alkylation reactions that occur on the acid sites of ZSM-5, the overall yield of aromatics is divided into two parts, namely, the "yield of aromatic rings" (A) and the "yield of alkyl groups on aromatic rings" (S_{C9+}). In a certain catalytic system, S_{C9+} and A exhibit a strong linear correlation under varying conditions. Therefore, the slope is defined as the "substitution ratio of the aromatic ring" (S_{C9+}/A) and is used as an indicator of the relative rate of alkylation to aromatization over the bifunctional catalyst. With similar acidic properties, the S_{C9+}/A value is revealed to be linearly dependent on the reciprocal of the b-axis length (1/b) of ZSM-5, which holds for both CO and CO_2-to-aromatics reactions (Fig. 21A). This linear dependency indicates that the straight channels parallel to the b-axis of ZSM-5 are the dominating generation and diffusion pathways for aromatic molecules, in other words, the spatial pathway for the aromatization and alkylation reactions. Accordingly, the aromatic distribution can be modulated by altering the crystal size of ZSM-5 along the b-axis.

A synthesis strategy for multi-component catalysts based on the recrystallization-induced component rearrangement and the construction of the directional spatial pathway for tandem reactions. Beginning with a mixed powder of metal oxide and zeolite, a typical binder of silica sol was introduced to obtain the extruded catalyst. Then, the extruded sample was treated by recrystallization under structure-directing agent steam to yield the final recrystallized sample, featuring an orient-distribution of the metal oxide and the zeolite.[117] More specifically, the metal oxide preferentially occupies the (100) and (101) surfaces of ZSM-5, thereby exposing the straight channels, which are the dominating generation and diffusion paths for aromatics. Consequently, a directional spatial pathway for the tandem reaction of CO_x to aromatics is achieved, facilitating the preferential diffusion of intermediates generated from metal oxide sites into ZSM-5 along adjacent sinusoidal channels, followed by their conversion into hydrocarbon products over acid sites, and finally the aromatic products smoothly diffuse out of the straight channels (Fig. 22B). Therefore, by construction of such a directional spatial pathway to match the diffusion and reaction of intermediates, a high catalytic efficiency can be achieved in the coupling of tandem reaction.

Designing the surface self-cleaning catalyst to improve the transfer efficiency of intermediates and boost the catalytic activity. The generation of intermediates on the surface of metal oxides provides the primary driving force for tandem reactions in metal oxide/zeolite coupling systems. However, for certain metal oxides, the intermediate may be converted into
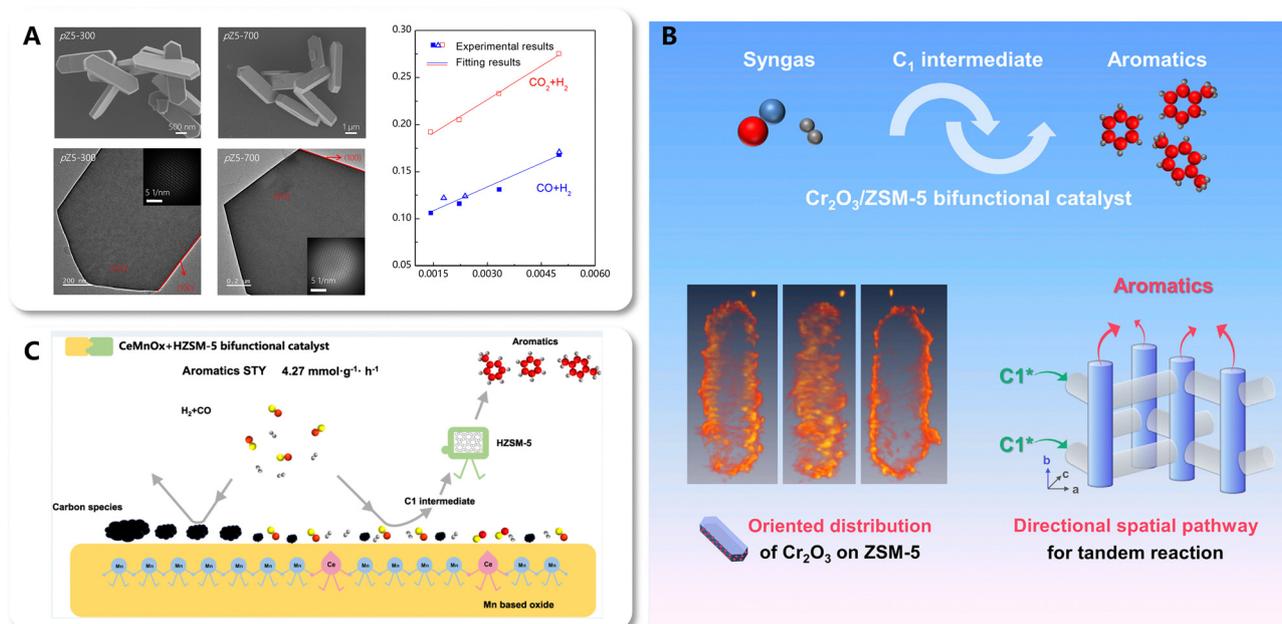
Fig. 22 (A) The correlation between aromatic distribution and key morphology parameters. Reprinted and reproduced with permission from Liu *et al.* Copyright (2020), American Chemical Society.[79] (B) directional spatial pathway based on orient-distributed metal oxide/zeolite catalysts. Reprinted with permission from Liu *et al.* Copyright (2021), Elsevier Inc.[117] (C) Surface self-cleaning effect of CeMnO$_x$ boosting the efficiency of the spatial pathway for the tandem reaction. Reprinted with permission from Zhang *et al.* Copyright (2024), American Chemical Society.[118]

long-chain hydrocarbons or even graphite carbon species, which will cover the metal oxide surface and inhibit further interaction of the intermediate with active sites. Regarding this problem, a modification strategy involving the doping of metal oxide with a second metal, such as doping MnO$_x$ with Ce, has been proposed. This strategy facilitates the removal of dissociated carbon species from the oxide surface by converting excess surface carbon species into short-chain hydrocarbons. Thus, the growth of graphite carbon species is suppressed, leading to the enhanced formation and transfer efficiency of intermediates, boosting the efficiency of the spatial pathway for the tandem reaction (Fig. 22C).[118]

6. Conclusions and prospects

Aromatics are important products of the traditional petrochemical industry, possessing a substantial market demand. The development of the technologies for direct conversion of CO$_2$ into aromatics aligns with the low-carbon transition of the chemical industry. Utilizing the strategy of coupling catalysis, two primary reaction pathways, specifically the methanol-mediated pathway and the modified Fischer–Tropsch pathway, have been intensively studied. The corresponding multi-functional catalysts, consisting of metal-based materials (metals, metal oxides or metal carbides) and zeolites, have achieved significant advancements, enabling the regulation and enhancement of CO$_2$ conversion and aromatic selectivity through the matching and synergy between catalytic components. Furthermore, several novel coupling pathways have been developed by integrating CO$_2$ hydrogenation with reactions

such as CO hydrogenation, aromatic alkylation, or alkane aromatization. Nonetheless, further development of technologies for direct aromatic production from CO$_2$ encounters three main challenges. First, the trade-off between CO$_2$ conversion and aromatic selectivity: the consumption of "green hydrogen" accounts for the major cost of the direct production of aromatics from CO$_2$, which is closely related to the product distribution. Precise selectivity control is therefore pivotal in enhancing the techno-economic viability of this process. Due to the complex reaction network, the methanol-mediated pathway exhibits high selectivity but relatively low activity, while the modified Fischer–Tropsch pathway is active yet demonstrates low selectivity to aromatics. The breakthrough of catalytic efficiency requires to overcome this trade-off effect. Second, the flexible and precise regulation of aromatic distribution: in the presence of the active intermediates, severe side reactions such as alkylation may arise and shift the aromatic distribution towards the heavy end, deviating from the market demand structure. Thus, it is essential to explore the flexible and precise regulation of aromatic distribution without compromising overall aromatic selectivity. Third, the scale-up engineering and industrial applications: in addition to the continuous deepening of understanding of catalytic mechanisms and structure–activity relationships, the iterative upgrading, scale-up engineering, and subsequent industrial applications have gained prominence, due to the increasing market demand and urgency for alternative aromatic production routes.

The key lies in the clarification, construction, and optimization of the coupling reaction pathways. Future research should focus on the following aspects: (1) enhancing the understanding of reaction mechanisms, completing the reaction networks,

elucidating the evolution of reaction species, in-depth characterization of catalytic activity sites, and subsequently exploring the quantitative influence of catalyst structural properties on tandem reactions; (2) developing environmentally friendly, efficient, and stable coupling catalytic systems through rational design and precise control of the location, distance, and orientation of the catalytic sites, thereby matching the adsorption and diffusion behaviors of intermediate species and boosting the tandem reaction efficiency through the directional spatial pathway; (3) expanding the coupling catalysis strategy and exploring novel coupling reaction pathways. In addition to the pathways discussed in this review, Wu *et al.* recently reported an FeMn&ZnCr&Z5@-SiO$_2$ catalyst for the conversion of CO in the presence of a low concentration of CO$_2$.[119] The enhancement in the space–time yield of PX is accomplished by coupling the methanol-mediated and Fischer–Tropsch pathways, representing a further exploration of the application of the coupling catalysis strategy in the aromatic production technology, using CO$_x$ as the carbon source; (4) scale-up engineering issues including macro-scale fabrication of multifunctional catalysts, process design dealing with intense thermal effects and complicated product separation, along with exploration of technology integration involving CO$_2$ capture and renewable hydrogen, ultimately aiming to provide novel technical solutions for efficient utilization of carbon resources and the advancement to a net-zero chemical industry. With the continuous development and expansion of the coupling strategy to drive the improvement of catalytic efficiency and product value, along with progress in renewable hydrogen production and carbon capture technology, the realm of CO$_2$ conversion to aromatics will demonstrate renewed vigor and vitality.

Data availability

The data that support the results of our work, in Fig. 22A, are available from the corresponding authors.

Conflicts of interest

There are no conflicts to declare.

Acknowledgements

References

1 IEA (2024), CO$_2$ Emissions in 2023, IEA, Paris https://www.iea.org/reports/co2-emissions-in-2023, Licence: CC BY 4.0.
2 Z. Liu, Z. Deng, S. Davis and P. Ciais, *Nat. Rev. Earth Environ.*, 2023, **4**, 205–206.
3 Y. Liu, D. Deng and X. Bao, *Chem*, 2020, **6**(10), 2497–2514.
4 D. Wang, Z. Xie, M. D. Porosoff and J. G. Chen, *Chem*, 2021, **7**(9), 2277–2311.
5 K. Cheng, Y. Li, J. Kang, Q. Zhang and Y. Wang, *Acc. Chem. Res.*, 2024, **57**(5), 714–725.
6 K. B. Tan, G. Zhan, D. Sun, J. Huang and Q. Li, *J. Mater. Chem. A*, 2021, **9**, 5197–5231.
7 G. Tian, X. Liang, H. Xiong, C. Zhang and F. Wei, *EES Catal.*, 2023, **1**, 677–686.
8 K. B. Tan, K. Xu, D. Cai, J. Huang and G. Zhan, *Chem. Eng. J.*, 2023, **463**, 142262.
9 X. Lu, K. B. Tan, J. Zhao and G. Zhan, *Chem. Catal.*, 2025, **5**(3), 101264.
10 W. Wang, C. Zeng and N. Tsubaki, *Green Carbon*, 2023, **1**(2), 133–145.
11 W. Dai, L. Yang, G. Wu, N. Guan and L. Li, in *Heterogeneous Catalysis for Sustainable Energy*, ed. L. Li and J. S. J. Hargreaves, WILEY-VCH GmbH, Weinheim, 2022, ch. 10, pp. 351–388.
12 I. Yarulina, A. D. Chowdhury, F. Meirer, B. M. Weckhuysen and J. Gascon, *Nat. Catal.*, 2018, **1**(6), 398–411.
13 I. M. Dahl and S. Kolboe, *J. Catal.*, 1996, **161**(1), 304–309.
14 I. M. Dahl and S. Kolboe, *J. Catal.*, 1994, **149**(2), 458–464.
15 M. Bjørgen, S. Svelle, F. Joensen, J. Nerlov, S. Kolboe, F. Bonino, L. Palumbo and S. Bordiga, *J. Catal.*, 2007, **249**(2), 195–207.
16 M. W. Erichsen, S. Svelle and U. Olsbye, *Catal. Today*, 2013, **215**, 216–223.
17 U. Olsbye, S. Svelle, M. Bjørgen, P. Beato, T. V. W. Janssens, F. Joensen, S. Bordiga and K. P. Lillerud, *Angew. Chem., Int. Ed.*, 2012, **51**(24), 5810–5831.
18 T. Sun, W. Chen, S. Xu, A. Zheng, X. Wu, S. Zeng, N. Wang, X. Meng, Y. Wei and Z. Liu, *Chem*, 2021, **7**(9), 2415–2428.
19 C. M. Wang, Y. D. Wang and Z. K. Xie, *J. Catal.*, 2013, **301**, 8–19.
20 W. Zhang, M. Zhang, S. Xu, S. Gao, Y. Wei and Z. Liu, *ACS Catal.*, 2020, **10**, 4510–4516.
21 A. Sassi, M. A. Wildman, H. J. Ahn, P. Prasad, J. B. Nicholas and J. F. Haw, *J. Phys. Chem. B*, 2002, **106**(9), 2294–2303.
22 M. Bjørgen, U. Olsbye and S. Kolboe, *J. Catal.*, 2003, **215**(1), 30–44.
23 M. Bjørgen, U. Olsbye, D. Petersen and S. Kolboe, *J. Catal.*, 2004, **221**(1), 1–10.
24 B. Arstad and S. Kolboe, *Catal. Lett.*, 2001, **71**(3–4), 209–212.
25 B. Arstad and S. Kolboe, *J. Am. Chem. Soc.*, 2001, **123**(33), 8137–8138.
26 W. Song, J. F. Haw, J. B. Nicholas and C. S. Heneghan, *J. Am. Chem. Soc.*, 2000, **122**(43), 10726–10727.
27 S. Ilias and A. Bhan, *ACS Catal.*, 2013, **3**(1), 18–31.
28 P. Gao, J. Xu, G. Qi, C. Wang, Q. Wang, Y. Zhao, Y. Zhang, N. Feng, X. Zhao, J. Li and F. Deng, *ACS Catal.*, 2018, **8**(10), 9809–9820.
29 M. Conte, J. A. Lopez-Sanchez, Q. He, D. J. Morgan, Y. Ryabenkova, J. K. Bartley, A. F. Carley, S. H. Taylor, C. J. Kiely, K. Khalid and G. J. Hutchings, *Catal. Sci. Technol.*, 2012, **2**(1), 105–112.
30 K. Cheng, W. Zhou, J. Kang, S. He, S. Shi, Q. Zhang, Y. Pan, W. Wen and Y. Wang, *Chem*, 2017, **3**(2), 334–347.
31 X. Yang, X. Su, B. Liang, Y. Zhang, H. Duan, J. Ma, Y. Huang and T. Zhang, *Catal. Sci. Technol.*, 2018, **8**(17), 4338–4348.

32 D. Liu, L. Cao, G. Zhang, L. Zhao, J. Gao and C. Xu, *Fuel Process. Technol.*, 2021, **216**, 106770.

33 D. B. Lukyanov, N. S. Gnep and M. R. Guisnet, *Ind. Eng. Chem. Res.*, 1995, **34**, 516–523.

34 G. Caeiro, R. H. Carvalho, X. Wang, M. A. N. D. A. Lemos, F. Lemos, M. Guisnet and F. Ramôa Ribeiro, *J. Mol. Catal. A:Chem.*, 2006, **255**(1–2), 131–158.

35 S. Kasipandi and J. W. Bae, *Adv. Mater.*, 2019, **31**(34), e1803390.

36 V. U. S. Rao and R. J. Gormley, *Catal. Today*, 1990, **6**(3), 207–234.

37 Y. Cheng, Y. Chen, S. Zhang, X. Wu, C. Chen, X. Shi, M. Qing, J. Li, C.-L. Liu and W.-S. Dong, *Green Chem.*, 2023, **25**(9), 3570–3584.

38 W. Zhou, S. Shi, Y. Wang, L. Zhang, Y. Wang, G. Zhang, X. Min, K. Cheng, Q. Zhang, J. Kang and Y. Wang, *ChemCatChem*, 2019, **11**(6), 1681–1688.

39 M. T. Arslan, B. A. Qureshi, S. Z. A. Gilani, D. Cai, Y. Ma, M. Usman, X. Chen, Y. Wang and F. Wei, *ACS Catal.*, 2019, **9**(3), 2203–2212.

40 P. Gao, S. Li, X. Bu, S. Dang, Z. Liu, H. Wang, L. Zhong, M. Qiu, C. Yang, J. Cai, W. Wei and Y. Sun, *Nat. Chem.*, 2017, **9**, 1019–1024.

41 Y. Ni, Z. Chen, Y. Fu, Y. Liu, W. Zhu and Z. Liu, *Nat. Commun.*, 2018, **9**(1), 3457.

42 Y. Xu, D. Liu and X. Liu, *Appl. Catal., A*, 2018, **552**, 168–183.

43 S. Guo, S. Fan, H. Wang, S. Wang, Z. Qin, M. Dong, W. Fan and J. Wang, *ACS Catal.*, 2024, **14**(1), 271–282.

44 L. Yang, C. Wang, W. Dai, G. Wu, N. Guan and L. Li, *Fundam. Res.*, 2022, **2**(2), 184–192.

45 M. T. Arslan, G. Tian, B. Ali, C. Zhang, H. Xiong, Z. Li, L. Luo, X. Chen and F. Wei, *ACS Catal.*, 2022, **12**(3), 2023–2033.

46 Y. Xu, J. Liu, J. Wang, G. Ma, J. Lin, Y. Yang, Y. Li, C. Zhang and M. Ding, *ACS Catal.*, 2019, **9**(6), 5147–5156.

47 Y. Xu, J. Wang, G. Ma, J. Lin and M. Ding, *ACS Sustainable Chem. Eng.*, 2019, **7**(21), 18125–18132.

48 B. Zhao, P. Zhai, P. Wang, J. Li, T. Li, M. Peng, M. Zhao, G. Hu, Y. Yang, Y.-W. Li, Q. Zhang, W. Fan and D. Ma, *Chem*, 2017, **3**(2), 323–333.

49 X. Cui, P. Gao, S. Li, C. Yang, Z. Liu, H. Wang, L. Zhong and Y. Sun, *ACS Catal.*, 2019, **9**(5), 3866–3876.

50 T. Li, T. Shoinkhorova, J. Gascon and J. Ruiz-Martínez, *ACS Catal.*, 2021, **11**(13), 7780–7819.

51 C. Wang, M. Hu, Y. Chu, X. Zhou, Q. Wang, G. Qi, S. Li, J. Xu and F. Deng, *Angew. Chem., Int. Ed.*, 2020, **59**(18), 7198–7202.

52 A. Hwang and A. Bhan, *Acc. Chem. Res.*, 2019, **52**(9), 2647–2656.

53 T. Wang, C. Yang, P. Gao, S. Zhou, S. Li, H. Wang and Y. Sun, *Appl. Catal., B*, 2021, **286**, 119929.

54 Y. Wang, W. Gao, S. Kazumi, H. Li, G. Yang and N. Tsubaki, *Chem. - Eur. J.*, 2019, **25**(20), 5149–5153.

55 Y. Wang, L. Tan, M. Tan, P. Zhang, Y. Fang, Y. Yoneyama, G. Yang and N. Tsubaki, *ACS Catal.*, 2019, **9**(2), 895–901.

56 L. Zhang, W. Gao, F. Wang, C. Wang, J. Liang, X. Guo, Y. He, G. Yang and N. Tsubaki, *Appl. Catal., B*, 2023, **328**, 122535.

57 K. Cheng, B. Gu, X. Liu, J. Kang, Q. Zhang and Y. Wang, *Angew. Chem., Int. Ed.*, 2016, **55**(15), 4725–4728.

58 J. Zhang, M. Zhang, S. Chen, X. Wang, Z. Zhou, Y. Wu, T. Zhang, G. Yang, Y. Han and Y. Tan, *Chem. Commun.*, 2019, **55**, 973–976.

59 X. Zhang, A. Zhang, X. Jiang, J. Zhu, J. Liu, J. Li, G. Zhang, C. Song and X. Guo, *J. CO₂ Util.*, 2019, **29**, 140–145.

60 Z. Li, Y. Qu, J. Wang, H. Liu, M. Li, S. Miao and C. Li, *Joule*, 2019, **3**(2), 570–583.

61 Y. Qu, Z. Li, H. Hu, S. Chen, J. Wang and C. Li, *Chem. Commun.*, 2023, **59**, 7607–7610.

62 C. Zhou, J. Shi, W. Zhou, K. Cheng, Q. Zhang, J. Kang and Y. Wang, *ACS Catal.*, 2020, **10**(1), 302–310.

63 H. Tian, P. Gao, X. Yang, C. Jiao, F. Zha, Y. Chang and H. Chen, *Chem. Eng. J.*, 2023, **466**, 143267.

64 B. Liu, Y. Wang, Y. Xie, L. Xiao, W. Wang and W. Wu, *ACS Sustainable Chem. Eng.*, 2023, **11**(49), 17340–17354.

65 Y. Yue, J. Tian, J. Ma, S. Yang, W. Li, J. Huang, Q. Li and G. Zhan, *Appl. Catal., B*, 2024, **355**, 124158.

66 E. Giamello, B. Fubini, M. Bertoldi, G. Busca and A. Vaccari, *J. Chem. Soc., Faraday Trans.*, 1989, **85**(2), 237–249.

67 M. Bertoldi, B. Fubini, E. Giamello, G. Busca, F. Trifirò and A. Vaccari, *J. Chem. Soc., Faraday Trans.*, 1988, **84**(5), 1405–1421.

68 G. D. Piero, F. Trifiro and A. Vaccari, *J. Chem. Soc., Chem. Commun.*, 1984, **10**, 656–658.

69 L. Tan, G. Yang, Y. Yoneyama, Y. Kou, Y. Tan, T. Vitidsant and N. Tsubaki, *Appl. Catal., A*, 2015, **505**, 141–149.

70 S. Tian, S. Wang, Y. Wu, J. Gao, Y. Bai, P. Wang, H. Xie, Y. Han and Y. Tan, *J. Mol. Catal. A:Chem.*, 2015, **404–405**, 139–147.

71 Q. Zhang, X. Li and K. Fujimoto, *Appl. Catal., A*, 2006, **309**(1), 28–32.

72 H. Song, D. Laudenschleger, J. J. Carey, H. Ruland, M. Nolan and M. Muhler, *ACS Catal.*, 2017, **7**(11), 7610–7622.

73 M. C. J. Bradford, M. V. Konduru and D. X. Fuentes, *Fuel Process. Technol.*, 2003, **83**(1–3), 11–25.

74 J. Wang, G. Li, Z. Li, C. Tang, Z. Feng, H. An, H. Liu, T. Liu and C. Li, *Sci. Adv.*, 2017, **3**, e1701290.

75 M. V. Frash and R. A. van Santen, *Phys. Chem. Chem. Phys.*, 2000, **2**(5), 1085–1089.

76 U. Lohse, B. Parlitz and V. Patzelovi, *J. Chem. Phys.*, 1989, **93**(9), 3677–3683.

77 N. O. Gonzales, A. T. Bell and A. K. Chakraborty, *J. Phys. Chem. B*, 1997, **101**(48), 10058–10064.

78 P. Zhang, L. Tan, G. Yang and N. Tsubaki, *Chem. Sci.*, 2017, **8**(12), 7941–7946.

79 C. Liu, J. Su, S. Liu, H. Zhou, X. Yuan, Y. Ye, Y. Wang, W. Jiao, L. Zhang, Y. Lu, Y. Wang, H. He and Z. Xie, *ACS Catal.*, 2020, **10**(24), 15227–15237.

80 W. Zhou, K. Cheng, J. Kang, C. Zhou, V. Subramanian, Q. Zhang and Y. Wang, *Chem. Soc. Rev.*, 2019, **48**(12), 3193–3228.

81 C. Yang, H. Zhao, Y. Hou and D. Ma, *J. Am. Chem. Soc.*, 2012, **134**(38), 15814–15821.

82 T. H. Pham, Y. Qi, J. Yang, X. Duan, G. Qian, X. Zhou, D. Chen and W. Yuan, *ACS Catal.*, 2015, **5**(4), 2203–2208.

83 M. E. Dry, *J. Chem. Technol. Biotechnol.*, 2001, **77**, 43–50.

84 F. Jiao, J. Li, X. Pan, J. Xiao, H. Li, H. Ma, M. Wei, Y. Pan, Z. Zhou, M. Li, S. Miao, J. Li, Y. Zhu, D. Xiao, T. He, J. Yang, F. Qi, Q. Fu and X. Bao, *Science*, 2016, **351**(6277), 1065–1068.

85 J. Zhu, P. Wang, X. Zhang, G. Zhang, R. Li, W. Li, T. P. Senftle, W. Liu, J. Wang, Y. Wang, A. Zhang, Q. Fu, C. Song and X. Guo, *Sci. Adv.*, 2022, **8**(5), eabm3629.

86 B. Yao, T. Xiao, O. A. Makgae, X. Jie, S. Gonzalez-Cortes, S. Guan, A. I. Kirkland, J. R. Dilworth, H. A. Al-Megren, S. M. Alshihri, P. J. Dobson, G. P. Owen, J. M. Thomas and P. P. Edwards, *Nat. Commun.*, 2020, **11**(1), 6395.

87 J. Wei, Q. Ge, R. Yao, Z. Wen, C. Fang, L. Guo, H. Xu and J. Sun, *Nat. Commun.*, 2017, **8**(1), 15174.

88 Y. Xu, C. Shi, B. Liu, T. Wang, J. Zheng, W. Li, D. Liu and X. Liu, *Catal. Sci. Technol.*, 2019, **9**(3), 593–610.

89 Y. Wang, S. Kazumi, W. Gao, X. Gao, H. Li, X. Guo, Y. Yoneyama, G. Yang and N. Tsubaki, *Appl. Catal., B*, 2020, **269**, 118792.

90 Y. Gu, J. Liang, Y. Wang, K. Huo, M. Li, W. Wang, R. He, S. Yasuda, X. Gao, G. Yang, M. Wu and N. Tsubaki, *Appl. Catal., B*, 2024, **349**, 123842.

91 J. Wei, R. Yao, Q. Ge, D. Xu, C. Fang, J. Zhang, H. Xu and J. Sun, *Appl. Catal., B*, 2021, **283**, 119648.

92 A. Ramirez, A. D. Chowdhury, A. Dokania, P. Cnudde, M. Caglayan, I. Yarulina, E. Abou-Hamad, L. Gevers, S. Ould-Chikh, K. D. Wispelaere, V. van Speybroeck and J. Gascon, *ACS Catal.*, 2019, **9**(7), 6320–6334.

93 G. Song, M. Li, P. Yan, M. A. Nawaz and D. Liu, *ACS Catal.*, 2020, **10**(19), 11268–11279.

94 G. Song, M. Li, L. Xu, X. Yang, M. A. Nawaz, H. Yuan, Z. Zhang, X. Xu and D. Liu, *Ind. Eng. Chem. Res.*, 2022, **61**(20), 6820–6830.

95 X. Yang, G. Song, M. Li, C. Chen, Z. Wang, H. Yuan, Z. Zhang and D. Liu, *Ind. Eng. Chem. Res.*, 2022, **61**(23), 7787–7798.

96 C. Chen, G. Song, Z. Wang, J. Song, Q. Jiang, Y. Zhai and D. Liu, *Appl. Catal., B*, 2024, **341**, 123330.

97 C. Chen, X. Li, Z. Wang, J. Song and D. Liu, *Chem. Eng. J.*, 2024, **483**, 149181.

98 G. Song, Q. Jiang, Y. Zhai and D. Liu, *Chem. Eng. Sci.*, 2023, **280**, 119037.

99 G. Song, Y. Zhai, Q. Jiang and D. Liu, *Fuel*, 2023, **338**, 127185.

100 Q. Jiang, G. Song, Y. Zhai, C. Chen, Z. Wang, H. Yuan, Z. Zhang and D. Liu, *Ind. Eng. Chem. Res.*, 2023, **62**(23), 9188–9200.

101 M. G. Sibi, M. K. Khan, D. Verma, W. Yoon and J. Kim, *Appl. Catal., B*, 2022, **301**, 120813.

102 G. Tian, Z. Li, C. Zhang, X. Liu, X. Fan, K. Shen, H. Meng, N. Wang, H. Xiong, M. Zhao, X. Liang, L. Luo, L. Zhang, B. Yan, X. Chen, H.-J. Peng and F. Wei, *Nat. Commun.*, 2024, **15**(1), 3037.

103 J. Zuo, W. Chen, J. Liu, X. Duan, L. Ye and Y. Yuan, *Sci. Adv.*, 2020, **6**(34), eaba5433.

104 Y. Lai, B. Hong, W. Zhou, D. Wen, Y. Xie, F. Luo, L. Ye, J. Zuo and Y. Yuan, *ACS Catal.*, 2024, **14**(15), 11780–11793.

105 R. Cao, T. Fu, Y. Liu, W. Qin, Y. Guo, C. Li, S. Huang and Z. Li, *ACS Catal.*, 2024, **14**(16), 12016–12030.

106 D. Miao, X. Pan, F. Jiao, Y. Ji, G. Hou, L. Xu and X. Bao, *Catal. Sci. Technol.*, 2021, **11**(13), 4521–4528.

107 C. Wei, W. Zhang, K. Yang, X. Bai, S. Xu, J. Li and Z. Liu, *Chinese J. Catal.*, 2023, **47**, 138–149.

108 J. Zuo, C. Liu, X. Han, D. Wen, X. Liu, L. Ye, W. Zhuang and Y. Yuan, *Chem. Catal.*, 2022, **2**(5), 1223–1240.

109 K. Bu, Y. Kang, Y. Li, Y. Zhang, Y. Tang, Z. Huang, W. Shen and H. Xu, *Appl. Catal., B*, 2024, **343**, 123528.

110 W. Chen, Y. Jiao, Y. Liu, M. Wang, F. Zhang and D. Ma, *CCS Chem.*, 2024, **6**, 1422–1429.

111 P. B. Weisz, *Adv. Catal.*, 1962, **13**, 137–190.

112 Y. Wang, G. Wang, L. I. van der Waals, K. Cheng, Q. Zhang, K. P. de Jong and Y. Wang, *Angew. Chem., Int. Ed.*, 2021, **60**(32), 17735–17743.

113 Y. Li, M. Wang, S. Liu, F. Wu, Q. Zhang, S. Zhang, K. Cheng and Y. Wang, *ACS Catal.*, 2022, **12**(15), 8793–8801.

114 W. Li, G. Zhan, X. Liu, Y. Yue, K. B. Tan, J. Wang, J. Huang and Q. Li, *Appl. Catal., B*, 2023, **330**, 122575.

115 Y. Ding, F. Jiao, X. Pan, Y. Ji, M. Li, R. Si, Y. Pan, G. Hou and X. Bao, *ACS Catal.*, 2021, **11**(15), 9729–9737.

116 C. Liu, S. Liu, H. Zhou, J. Su, W. Jiao, L. Zhang, Y. Wang, H. He and Z. Xie, *Appl. Catal., A*, 2019, **585**, 117206.

117 C. Liu, J. Su, Y. Xiao, J. Zhou, S. Liu, H. Zhou, Y. Ye, Y. Lu, Y. Zhang, W. Jiao, L. Zhang, Y. Wang, C. Wang, X. Zheng and Z. Xie, *Chem. Catal.*, 2021, **1**(4), 896–907.

118 L. Zhang, J. Su, C. Liu, S. Liu, H. Zhou, W. Jiao, Y. Hu, F. Xiong, Y. Lu, Y. Ye, X. Zheng, Y. Zhang, Y. Wang and H. He, *ACS Catal.*, 2024, **14**(11), 8972–8982.

119 X. Wu, C. Wang, S. Zhao, Y. Wang, T. Zhang, J. Yao, W. Gao, B. Zhang, T. Arakawa, Y. He, F. Chen, M. Tan, G. Yang and N. Tsubaki, *Nat. Commun.*, 2024, **15**(1), 8064.